# Disentangling the compositional variations of lawsonite in blueschist-facies metasediments (Schistes Lustrés, W. Alps)

Benjamin Lefeuvre, Benoît Dubacq, Anne Verlaguet, Clément Herviou, Stephanie Walker, Benoît Caron, Ethan Baxter, Philippe Agard

# Disentangling the compositional variations of lawsonite in blueschist-facies metasediments (Schistes Lustrés, W. Alps)

Benjamin Lefeuvre[1,2*], Benoît Dubacq[1], Anne Verlaguet[1], Clément Herviou[1,3,4], Stephanie Walker[5], Benoît Caron[1], Ethan Baxter[5], Philippe Agard[1]

[1] Sorbonne Université, CNRS-INSU, Institut des Sciences de la Terre de Paris, ISTeP UMR 7193, F 75005 Paris, France

[2] Laboratoire des Fluides Complexes et leurs Réservoirs – IPRA, E2S-UPPA, TotalEnergies, CNRS, Université de Pau et des Pays de l'Adour, UMR5150 Pau, France

[3] Department of Earth, Marine and Environmental Sciences, University of North Carolina, Chapel Hill, NC 27599-3315, USA

[4] Université de Lyon 1, CNRS UMR5276, ENS de Lyon, LGL-TPE, Villeurbanne Cedex, France.

[5] Department of Earth and Environmental Sciences, Boston College, 140 Commonwealth Ave, Chestnut Hill, MA02467, USA

*Corresponding author: benjamin.lefeuvre@univ-pau.fr

Keywords: lawsonite, metasediments, fluid/mass transfer, Schistes Lustrés, REE (LA-ICP-MS), Strontium isotopes (TIMS)

## *Abstract*

*Lawsonite is important as a carrier of $H_2O$ in subduction zones and as a petrological tracer. The trace element content of lawsonite in mafic rocks has been used as a record of fluid-rock interactions but has received less attention in metamorphosed oceanic sediments. This study documents the major and trace element composition, together with $^{87}Sr/^{86}Sr$ isotopic ratios, of the different lawsonite types identified in the upper units of the Schistes Lustrés complex of the Western Alps, a paleo-accretionary prism of the Liguro-Piemont slow-spreading ocean subducted up to 40 km. The lawsonite-rich upper units of the Schistes Lustrés complex are principally composed of metamorphosed pelitic sediments and carbonates. Lawsonite content reaches 40 vol.% in the rock matrix and in veins. All lawsonite types originate from prograde metamorphic reactions which occurred up to peak metamorphism. Lawsonite compositions have been measured in-situ with electron microscopy, microprobe and laser-ablation mass spectrometry. Lawsonite separates have been measured for Sr content and $^{87}Sr/^{86}Sr$ isotopic ratios using TIMS. Bulk rock compositions have been measured with ICP-OES and ICP-MS. Analysis contamination by minute retrograde white mica inclusions in lawsonite crystals precluded using univalent cations for petrological interpretations. For other trace elements, the variability of lawsonite appears extremely high, with crystal compositions varying between samples and between crystals in individual samples. However, clear patterns emerge between lawsonite types, reflecting equilibrium and out-of-equilibrium processes unrelated to pressure-temperature conditions. At crystal scale, textural hourglass zoning predominates in lawsonite from the schist, while growth zoning is found in both schists and veins. The combination of both mechanisms results in spectacular zoning in Ti and in rare earth element contents spanning four orders of magnitude. Over time, the La/Yb ratio decreases strongly (from ~100 to ~1), as La appears much more sensitive to surface effects leading to textural hourglass zoning. Interface-coupled dissolution-precipitation also contributes to decoupling of less mobile elements in the schist. This is best observed for Ti, but rare earth element and chromium contents are affected too. These processes are considered to occur near closed-system conditions. Late lawsonite overgrowths with higher Sr contents are interpreted as reflecting system opening in the veins, yet sometimes observed in the schists. Strontium isotopic ratios measured on separated lawsonite crystals and on bulk rocks also show very large spreads. This indicates that the system did not equilibrate during blueschist-facies metamorphism, due to bulk rock heterogeneities during deposition and limited mineral reactivity at the local scale. Strontium isotopic ratios do not correlate with Sr content which rules out limestone devolatilization as the main driver of lawsonite overgrowths. In places, lawsonite is far more radiogenic than the host rocks, indicating either the destabilization of local Rb-rich phases (such as mica, illite and smectite) or the infiltration of externally-derived fluids. The overall compositional evolution of lawsonite records incremental system opening. However, lawsonite offers no evidence of large-scale mass transfer and external fluid influx in the Schistes Lustrés complex, even though the vein network is abundant and extends over time.*

## INTRODUCTION

Sediments undergoing subduction contain large amounts of $H_2O$ (up to 7 wt. % entering the trench globally, Plank and Langmuir, 1998; Plank, 2014) and release water via metamorphic reactions through burial (e.g., Schmidt and Poli, 1998; Hacker et al., 2003; Van Keken et al., 2011). At depth, fluids play a major role as their migration induces dramatic changes in the mechanical and chemical properties of rocks. The amount of fluids (e.g., $H_2O$, $CO_2$) produced can be estimated (e.g., via thermodynamic modeling as by Hacker and Abers, 2004; Baxter and Caddick, 2013; Ague and Nicolescu, 2014; Kleine et al., 2014; Piccoli et al. , 2021, among many others), but pathways and scales of fluid migration remain hard to assess, especially in sedimentary lithologies where alternating horizons show hugely variable permeability, and where connection of vein networks may be transient and poorly recorded. Trace elements, fluid inclusions and/or isotopic signatures of minerals growing in subducted rocks, metamorphic veins or shear zones are useful tracers of fluid migration during prograde metamorphism. Lawsonite is of particular interest as it is stable over an extended pressure-temperature range (Schmidt and Poli, 1994), generally growing as prisms, and can be locally abundant. Lawsonite is also intimately linked to both the water and carbon cycles as a it is a major $H_2O$ host (~12 wt. %) and its formation reactions involve devolatilization and dissolution/crystallization of carbonates (Nitsch, 1972; Cook-Kollars et al., 2014; Lefeuvre et al., 2020).

Lawsonite has been shown to be remarkably stable around its ideal composition ($CaAl_2Si_2O_7(OH)_2.H_2O$) regardless of pressure-temperature conditions (e.g., Okamoto and Maruyama, 1999), but it can host various trace elements. Lawsonite incorporates Pb, Sr and rare earth elements (REE), especially light rare earths (LREE), preferentially to other minerals in classical assemblages (e.g., reviews in Fornash et al., 2019; Whitney et al., 2020; Kang et al., 2022). Previous studies of the minor and trace element composition of lawsonite in mafic blueschists, eclogites, and metasomatic rocks have shown that variations of lawsonite composition may reflect reactions between trace element-rich minerals and/or changes in fluid compositions, with implications for element cycling in shallow to deep parts of subduction zones (e.g., Tribuzio et al., 1996; Ueno, 1999; Spandler et al., 2003; Tsujimori et al., 2006; Martin et al., 2011, 2014; Vitale Brovarone et al., 2014; Vitale Brovarone and Beyssac, 2014; Fornash et al., 2019; Whitney et al., 2020; Kang et al., 2022).

Studies on metasedimentary lawsonite are scarce (Martin et al., 2014; Whitney et al., 2020), although lawsonite is abundant in blueschist-facies calcschists such as in the Schistes Lustrés (SL) complex of the Western Alps, where lawsonite locally represents up to 40 vol.% of the metasediments (Agard et al., 2001; Lefeuvre et al., 2020; Manzotti et al., 2021). The SL units correspond to fragments of oceanic lithosphere successively buried along a cold geothermal gradient (~ 8°C/km, Agard et al., 2001; Agard, 2021; Herviou et al., 2022) during Alpine subduction, exhumed sliced from the downgoing plate at

various depths. The SL provide a well-exposed example of a deep accretionary complex (Platt, 1986; Marthaler and Stampfli, 1989; Agard et al., 2009; 2018; Agard, 2021). Metasediments are volumetrically dominant and crop out continuously over large distances, allowing studies of the production, composition and behavior of fluids in subducted sediments (Agard et al., 2000; Bebout et al., 2013; Herviou et al., 2021). Oxygen and carbon isotopic data in the metasediments suggest that most of the fluid present during subduction was locally-derived (Henry et al., 1996; Bebout et al., 2013; Cook-Kollars et al., 2014; Jaeckel et al., 2018; Epstein et al., 2020), consistently with the composition of fluid inclusions in carpholite and lawsonite-bearing veins (Agard et al., 2000; Herviou et al., 2021; see also Raimbourg et al., 2018; Lefeuvre, 2020). Therefore, metasediments of the SL complex mostly behaved as a rock-buffered system, with volumetrically large but transient and restricted fluid migration. External fluid infiltration was limited, but the scales of fluid migration and element mobility remain poorly known. Lawsonite is found in these rocks in pelitic layers and in a network of high-pressure veins, locally with carpholite (Agard et al. 2000, 2001; Vitale Brovarone et al., 2020; Lefeuvre et al., 2020; Herviou et al., 2021, 2023; Manzotti et al., 2021). Lawsonite is thought to grow during prograde metamorphism of the SL units, with veins providing evidence for incremental lawsonite growth during crack-seal events (Herviou et al., 2023). Do trace element compositional variations in lawsonite record variations in fluid signature along the prograde path?

In light of the very large variability of minor and trace element composition of lawsonite (Fornash et al., 2019; Whitney et al., 2020; Kang et al., 2022), this study provides a petrological model to refine the crystallization history of lawsonite and to shed light over the scale of element mobility during prograde and peak metamorphism at blueschist-facies conditions. To address these questions, lawsonite crystals from the SL calcschists and high-pressure veins have been analyzed for major and trace elements, coupled to bulk rock analyses and strontium isotopic analyses on bulk samples and on lawsonite separates.

## GEOLOGICAL SETTING AND PREVIOUS WORK

### The Schistes Lustrés complex in the Western Alps

The Western Alps result from an east-dipping, slow and cold subduction (~8°C/km at a maximum of 2 cm/year) of the Valais and Liguro-Piemont slow-spreading oceans below Adria/Apulia microcontinents (Le Pichon et al., 1988; Lagabrielle and Cannat, 1990; Agard et al., 2001; Lapen et al., 2003; Schmid et al., 2017). Subduction of these slow-spreading oceanic domains lasted around 60 Myr (Stampfli et al., 1998; Agard, 2021) and was followed by continental subduction and collision (e.g., Mendes et al., 2023).

Remnants of Liguro-Piemont oceanic lithosphere are now exposed in the internal domain of the Western Alps and form a nappe-stack known as the Liguro-Piemont domain or SL complex (Caron, 1974; Lagabrielle and Lemoine, 1997; Agard et al., 2001, 2002; Agard, 2021; Herviou et al., 2022) owing to their characteristic sedimentary features (Fig. 1a; for more details on the overall Alpine structure, see: Coward and Dietrich, 1989; Lagabrielle and Lemoine, 1997; Rosenbaum and Lister, 2005; Handy et al., 2010). Former oceanic sediments (marls, shales and limestones, e.g., Lemoine, 2003) correspond to an initial ~200-400 meter thick sequence of Upper Jurassic to Upper Cretaceous pelagic and hemipelagic seafloor deposits (De Wever and Caby, 1981; Lemoine et al., 1984; Lemoine and Tricart, 1986; Deville, 1986; Deville et al., 1992; Lemoine, 2003). Minor and variable amounts of mafic and ultramafic rocks are also found in the SL complex (e.g., Lagabrielle et al., 2015; Herviou et al., 2022).

During subduction, fragments of the Liguro-Piemont oceanic lithosphere were successively scraped off the downgoing plate, stacked at depths and exhumed to form a deep accretionary complex built by progressive underplating (Platt, 1986; Marthaler and Stampfli, 1989; Agard et al., 2009; 2018; Agard, 2021; Agard and Handy, 2021; Plunder et al., 2012., Herviou et al., 2022). Several units corresponding to independent subduction slices were identified in the SL complex (Lagabrielle, 1987; Fudral, 1996; Tricart and Schwartz, 2006; Lagabrielle et al., 2015). Herviou et al. (2022) reappraised the overall structure of the complex, highlighting a trimodal distribution of units with near-continuous eastward increase in peak burial conditions from the Liguro-Piemont Upper units (LPU; 320-400°C – 1.2-1.9 GPa) to the Middle units (LPM; 415-475°C – 1.7-2.2 GPa) and to the Lower units (LPL; 500-580°C – 2.2-2.8 GPa; Fig. 1c; for peak metamorphic conditions through the domain see also Agard et al., 2001; Beyssac et al., 2002; Gabalda et al., 2009; Plunder et al., 2012; Angiboust et al., 2012; Schwartz et al., 2013; Locatelli et al., 2018). The LPU and LPM units metamorphosed under blueschist-facies conditions are dominated by sediments (> 90 %), whereas the LPL units metamorphosed at eclogite-facies conditions are richer in mafic-ultramafic rocks (> 40 %; Herviou et al., 2022).

## Lawsonite-bearing calcschists on the Cottian Alps transect

This contribution focuses on lawsonite-bearing calcschists from the LPU unit of the Cottian Alps (Lago Nero slice; Polino et al., 2002; Herviou et al., 2022) and more specifically on the Strada dell'Assietta transect (Caron, 1974; Lefeuvre et al., 2020; Fig. 1b) between Fraiteve and the Assietta pass, along a ~15 km SW-NE traverse in the French-Italian Cottian Alps (Fig. 1b, c; Caron, 1974; Polino, 1984). Metasediments recorded four deformation stages described by Agard et al. (2001; 2002) and Ghignone et al. (2020). Kilometer-scale folding associated with thin-skinned stacking during blueschist-facies peak burial (D1) is dated at 62-55 Ma. These early fabrics have been largely erased by a D2 event (51-45 Ma) with top-to-the-east shear deformation patterns associated with early exhumation under blueschist-facies, and by subsequent west-vergent shear zones (D3) associated with greenschist facies

conditions (38-35 Ma; Agard et al., 2002). Late normal faults characterize the final ductile-brittle transition during late exhumation. The metasediments along the transect are composed of alternations of carbonates and pelitic horizons (Fig. 1d, e), which are of varying thickness and proportions, ranging from pelites (described as type 1 calcschists by Lefeuvre et al., 2020, Fig. 1d, e) to thick carbonate beds almost lacking pelitic horizons (type 5 in Lefeuvre et al., 2020, Fig. 1d, e).

Lawsonite is the dominant hydrous phase stable at peak conditions in LPU metasediments, but its distribution is very heterogeneous. Lawsonite growth has been described as 'massive' by Lefeuvre et al. (2020) because it amounts to about half the volume of large outcrops in the LPU units in type 3 calcschists, but it is restricted to fine carbonate-metapelite mixtures (also ubiquitous in type 3 calcschists) that allow reaction between Ca, Al, Si and $H_2O$. Four textural occurrences of lawsonite were identified by Lefeuvre et al. (2020) and were labelled from A to D (LwsA, LwsB, LwsC, LwsD) without implying chronological order. In thin pelitic horizons, lawsonite occurs as millimetric black prisms coined LwsA, by far the most abundant lawsonite type. Cream-colored lawsonite fibers labelled LwsB are found in decimeter to meter-long quartz-rich veins elongated parallel to vein walls and recording incremental crack-seal growth (Fig. 2f; Herviou et al., 2023). LwsC-bearing centimetric tensile veins contain cream-colored lawsonite fibers in textural equilibrium with ankerite and quartz, all growing perpendicular to vein walls. LwsA in the schist is interpreted as the product of the prograde reaction chlorite + aragonite + kaolinite = lawsonite + ankerite + quartz + $H_2O$, beginning at conditions possibly as low as 0.4 GPa/180 °C (Lefeuvre et al., 2020). Lawsonite veins likely formed all along the prograde path, in response to pressure-solution processes. While LwsC veins likely opened as single stage, short-lived tensile events, LwsB incremental crack-seal fibers may have recorded longer-lived events along the prograde path (Lefeuvre et al., 2020; Herviou et al., 2023). LwsD is restricted in pelitic layers and occurs as white rosette-like prisms in the schist (Fig. 2g). Table 1 presents the mineralogy, rock and lawsonite types for all samples.

## LAWSONITE OCCURRENCE, TEXTURE AND ASSOCIATED MINERALOGY

This study focuses on three representative lawsonite-bearing outcrops along the Strada dell'Assietta transect (Fig. 1): Desertes, Triplex and Assietta. The Fraiteve location also offers an interesting outcrop of the least metamorphosed rocks of the series. At the 200m long Mt. Triplex outcrop, lawsonite is particularly abundant in both schist and veins (Fig. 2). These type 2 (and type 3 to a lesser extent) calcschists are made of pelitic and carbonate-rich layers alternating every few centimeters, highly folded and affected by D2-related penetrative shear bands. D2 shear structures are cross-cut by later west-vergent D3 shear bands (Fig. 2a, b).

LwsA crystallized in the thin pelitic layers as millimetric to centimetric black prisms enriched in organic matter (OM). LwsA is systematically associated reddish oxidized ankerite found at the

interface between pelitic and carbonate-rich beds (Figs. 2b, c, 3a). Samples Tpx-A1, Tpx-A2 and Tpx-A3 (Table 1) contain large amounts of centimetric LwsA crystals reaching 40 vol. % of the whole rock (Fig. 3a, b), and are hereafter referred to as 'host calcschists' (Figs. 2c, 3). LwsA in pelite-rich layers is closely associated with ankerite and quartz (Fig. 3c, d, e, f). Fine mixtures of phengite, chlorite and calcite are surrounding LwsA crystals and interpreted as the retrograde assemblage of lawsonite destabilization (Fig. 3c, e; Sicard-Lochon and Potdevin, 1986). Accessory minerals are scarce in the host calcschists; tiny rutile needles were identified in lawsonite, and apatite occurs in one sample (Fig. 3f; Tpx-A2). Optical microscopy reveals complex growth patterns for LwsA. Differences in interference colors under crossed polars clearly indicates the presence of hourglass zoning (Fig. 3b, e). In some LwsA crystals, organic matter (OM) inclusions help to illuminate the zoning and identify the hourglass shapes (Fig. 3b). Such chemical zoning has been previously described in metasedimentary lawsonite (Vitale Brovarone et al., 2014; Fornash et al., 2019; Whitney et al., 2020). LwsA cores include OM in trails aligned along crystal faces (Fig. 3c, d), folded and rotated compared to the surrounding schistosity, or highlighting hourglass zoning (Fig. 3c, e). These OM-rich cores are generally rimmed by OM-free lawsonite (Fig. 3b, c, e), suggesting a series of discrete growth events of LwsA (see Rice and Mitchell, 1991 for details about textural zoning and carbon-rich inclusion bands).

Rare white crystals of prismatic lawsonite, without preferential orientation, are observed in pelitic layers in the vicinity of LwsB-bearing veins. These have been classified as a fourth lawsonite type: LwsD. LwsD is present in sample Tpx-D1 (Fig. 2e, g) collected 1 meter away from LwsB-bearing Tpx-B1, and in Ft-D1 collected in Fraiteve. As with LwsA, LwsD crystals are locally associated with ankerite and quartz (Fig. 2g), and partially retrogressed by phengite, chlorite and calcite. LwsD contains little OM inclusions compared to LwsA.

Veins are abundant, especially at Mt. Triplex where they have been estimated to make up to 30 % of the outcrops (Herviou et al., 2023). LwsB-bearing veins are decimeter to meter-long, parallel to the main D1/D2 schistosity, ductility deformed (Fig. 2b, f). LwsB-bearing veins collected at Triplex and at Desertes (Table 1, Tpx-B1, Tpx-B2, Ds-B2, Ds-B3) are composed of quartz and fibers of cream-colored LwsB often fractured and systematically elongated parallel to vein walls (Fig. 4a-c), highlighting their formation by dilatational shearing (Herviou et al., 2023). Ankerite crystals were found at the selvages of some veins but are rarely observed in association with LwsB (Fig. 4a). LwsB crystals do not contain OM but are often pseudomorphed into a mixture of phengite and chlorite (Fig. 4b, c).

LwsC-bearing veins are millimetric to centimetric tensile veins crosscutting the schistosity. These veins occur in the vicinity of fold hinges, close to LwsB-bearing veins, and are only found where LwsA is widespread in the schist. LwsC fibers are associated with ankerite and quartz, all growing perpendicularly to the vein selvages (Fig. 4d-f). LwsC-bearing veins are easily missed as they are small, scarce, largely sheared and poorly preserved. In most veins, LwsC fibers are pseudomorphed into

phengite, chlorite and calcite (Fig. 4f). The freshest LwsC veins, selected for the geochemical study, were found in the vicinity of the 'multiquartz aggregates' described below. Herviou et al. (2023) have shown that the emplacement of the lawsonite vein (LwsB and LwsC) network is continuous and incremental, interpreted as the fossil record of slow slip events. The relative chronology between these events is therefore complicated to establish as the formation of these veins can be related to multiple processes.

In places, lawsonite-bearing veins are clustered and intimately folded and sheared with the surrounding schist, resulting in intricate patterns with schistose fragments embedded in high-pressure veins with abundant quartz (Figs. 2d, e). These objects, referred to as 'multiquartz aggregates', were sampled both in Triplex (Tpx-AB5 and Tpx-AC4) and Assietta pass (As-AB1 and As-AC2). Lawsonite in these schistose fragments is therefore in direct proximity (< 1 cm) to lawsonite growing in the embedding veins. Lawsonite in schistose fragments (noted LwsA*) forms black prisms including OM trails, similar to those observed elsewhere in the schist, crystallizing with quartz and ankerite (Sup. Mat. 1a-c). Veins contain elongated lawsonite fibers similar to LwsB (labelled LwsB*; Figs. 2e, 5a-d), showing multiple growth steps synchronous with deformation (Figs. 2e, Sup. Mat. 1a, c). LwsB* crystals are associated with quartz and are very often pseudomorphosed into phengite and chlorite (Sup. Mat. 1c, d). Some multiquartz aggregates display LwsC tensile veins (Figs. 2d, Sup. Mat. 1f), generally at the interface between LwsB*-bearing veins and embedded schistose fragments (Fig. 2e). LwsC fibers are associated with quartz and oxidized ankerite (Sup. Mat. 1g) and are well-preserved compared to LwsC in most veins elsewhere and were therefore selected for analysis (Tpx-AC4, As-AC2).

## ANALYTICAL METHODS

### Analytical strategy (Table 1)

Major and trace element analysis have been carried out in lawsonite crystals to study whether lawsonite and its zoning patterns record evolving length-scales of element mobility and fluid circulation. Thick sections were made on 20 lawsonite-bearing samples (Table 1) to perform laser ablation ICP-MS and X-ray chemical maps to measure lawsonite trace element content and distribution.

Ten rock samples were selected along the Strada dell'Assietta transect (Fig. 5a) for bulk measurements. Nine of them are calcschists, representative of the types identified by Lefeuvre et al. (2020; Fig. 2a, b). One pelitic (Desertes; type 1) and one carbonate-rich calcschist (Gleise; type 4) were selected to represent end-member lithologies, where lawsonite is not abundant. Most samples (7) were selected in type 2 and type 3 calcschists (Fig. 2a, b) in which lawsonite is widespread (Lefeuvre et al., 2020). In order to identify potential interactions with mafic rocks, one ~10 m long basaltic pillow breccia

body embedded in the calcschists was sampled at the Bourget site (Bg-mafic; 20 m away from the Bourget calcschist sample) and analyzed.

Strontium isotopic ratios were measured on mineral separates and selected bulk samples because Sr is commonly enriched in both carbonates and lawsonite (Enami, 1999; Martin et al., 2014; Hara et al., 2019; Whitney et al., 2020) and rather mobile in aqueous fluids, therefore useful to study fluid-rock interactions (see Hara et al., 2018).

### Bulk-rock geochemistry (Table 2)

Samples were finely crushed (< 2µm) in an agate mortar. Sample powders were weighed and heated for 1h at 1100°C to ensure destruction of OM. Powders were dissolved at 80°C in closed beakers with $HNO_3$ and HF overnight. For analysis of major elements, $B(OH)_3$ was introduced quickly after opening the beakers to avoid loss of silica. Further dilution was carried out with 2% $HNO_3$ before analysis. Major and trace element compositions were analyzed at ALIPP6 (ISTeP, Sorbonne Université, Paris) using an ICP-OES spectrometer (Agilent 5100 HVDV) for major elements and an ICP-MS/MS (Agilent 8800) for trace elements. Calibration was made using a set of international and in-house standards (RGM-1, BIR-1, AGV-2, LIP, M77-2, GSN, COS, BHVO-2). To characterize the major element budget of these rocks, 10 oxides were measured ($SiO_2$, $TiO_2$, $Al_2O_3$, FeO, MnO, MgO, CaO, $Na_2O$, $K_2O$ and $P_2O_5$). A total of 37 minor and trace elements were selected for this study (Li, Be, Sc, V, Cr, Co, Ni, Cu, Zn, Ga, As, Rb, Sr, Y, Zr, Nb, Cs, Ba, Ta, Pb, La, Ce, Pr, Nd, Sm, Eu, Gd, Tb, Dy, Ho, Er, Tm, Yb, Lu, Hf, Th and U).

### Major element analysis and chemical mapping of lawsonite (Tables 3, 4, 5, 6)

Major element analysis of lawsonite crystals has been carried out at CAMPARIS (Sorbonne Université, Paris) with a CAMECA SX-Five electron microprobe and the data reduction method of Pouchou and Pichoir (1991). Analytical conditions were 15 kV-10 nA in WDS mode for analysis of major elements. Conditions were changed to 25 kV-100 nA when measuring minor elements (Sr, Ti, and Cr). $Fe_2O_3$ (Fe), $MnTiO_3$ (Mn, Ti), diopside (Mg, Si), $Cr_2O_3$ (Cr), SrSi (Sr), orthoclase (Al, K), anorthite (Ca) and albite (Na) were used as standards for calibration of elements in parentheses. Quantitative mapping was performed using the same analytical conditions in WDS mode. Qualitative element mapping was also carried out with a SUPRA-55VP SEM at ISTeP (Sorbonne Université, Paris) in energy-dispersive spectroscopy (EDS) mode at 15 keV acceleration voltage, 30 nA beam current with a dwell time of 256 µs, analyzing each area up to 10 times for increased signal/noise ratio.

### Trace element analysis of lawsonite (Table 7)

Trace element lawsonite concentrations were measured at ALIPP6, using a laser ablation ICP-MS/MS (Teledyne Analyte G2 193 nm ArF excimer laser ablation system coupled to an Agilent 8800 ICP-MS/MS) on polished thick sections (100 µm). Lawsonite crystals were ablated for 60 s (frequency of 8 Hz) in a He atmosphere using a 40 µm beam and a laser fluency of 3.54 J/cm$^2$. Background was measured 18 s before and after sampling ablation. Standardization was carried out using BCR2-G international glass standard, and $^{27}$Al as internal standard obtained from electron microprobe analyses. Instrument drift and accuracy were controlled with repeated analyses of the international standards ATHO-G and BHVO2-G. Every ablation pattern was verified with an in-house spreadsheet to check for absence of impurities and/or inclusions during ablation (89 out of 400 analyses were discarded).

## Strontium isotopic ratios (Table 8)

Lawsonite strontium isotopic ratios were determined at the Boston College Center for Isotope Geochemistry using an IsotopX Phoenix Thermal Ionization Mass Spectrometer (TIMS). First, lawsonite crystals were separated from the bulk rock after crushing and sieving (see Sup. Mat. 2). Mineral fractions between 500µm and 125µm were separated using sodium polytungstate (density of 2.9 g.cm$^{-3}$) allowing isolation of the heavy fraction containing lawsonite, ankerite and oxides. Lawsonite grains were separated using magnetic separation, cleaned in ultrasonic baths and handpicked before dissolution for TIMS analysis. Dissolution followed a four-step protocol (Sup. Mat. 2). Lawsonite separates were partially dissolved in 2mL of glacial acetic acid in an ultrasonic bath to remove remaining carbonates. This first step was repeated twice to purify the lawsonite fraction. Samples were subsequently dissolved in HF-$HNO_3$-HCl. Cleaned lawsonite fractions were attacked with 100 µL of HF together with 2 mL of $HNO_3$ at 120°C overnight. After 12 hours, the sample was dried down. The same step was repeated with 2 mL of $HNO_3$ at 120°C. Dissolved samples were prepared for chemistry in 2 mL of HCl at 120°C. Strontium was separated using 100 µL micro-columns and pre-cleaned Sr-spec resin. Approximately 100 ng of Sr were loaded onto Re filaments with a TaF activator solution. Samples were analyzed using a multidynamic method, and repeated analysis of Sr standard SRM987 during the duration of the project gave 0.710240 ± 0.000010 (n = 5; 2sd), which is within the long-term average of 0.710242 ± 0.000005 (n=114; 2sd).

This procedure has been applied to bulk rock samples (without preliminary partial dissolution). In total, 7 bulk rocks and 17 lawsonite separates have been analyzed (8 LwsA, 6 LwsB, 1 LwsC and 2 LwsD samples). These same dissolved lawsonite samples were also aliquoted for ICP-MS analysis to determine the Sr and Rb concentrations and $^{87}$Rb/$^{86}$Sr ratios reported in Table 8. Uncertainty in $^{87}$Rb/$^{86}$Sr is 2.8 % RSD based on repeat analysis of standard solutions.

## RESULTS

### Bulk rock geochemistry

Bulk rock compositions reflect the petrographic variability of the metasediments along the Strada dell'Assietta transect (Fig. 1d-e; Table 2): compositions evolve gradually in ACF ($Al_2O_3$-CaO-FeO; Fig. 5a) space between pelitic horizons (Desertes, lithology type 1 in Fig. 1d-e) and carbonate-rich endmembers (Gleise, lithology type 4 in Fig. 1d-e). These rocks exhibit similar FeO contents around 20 % in ACF except for the mafic sample (Bg-mafic) described below. CaO and $Al_2O_3$ contents are inversely correlated (Fig. 5b). Pelitic horizons (Desertes; type 1) contain > 25 wt. % of $Al_2O_3$ and < 10 wt. % of CaO, whereas carbonate-rich calcschists (Gleise; type 4) contain up to 58 wt. % of CaO and ~5 wt. % of $Al_2O_3$. Type 2 calcschists contain between 15 and 25 wt. % of $Al_2O_3$ and 10-25 wt. % of CaO, whereas more carbonated type 3 calcschists contain 7 to 15 wt. % of $Al_2O_3$ and 25 to 50 wt. % of CaO. At first order, $TiO_2$ and Ce are anti-correlated to CaO content (as for $Al_2O_3$), but Sr is positively correlated to CaO content (Fig. 5b). $TiO_2$ is a major component of the SL calcschists (ranging between 0.1 and 1.9 wt. %) and is more concentrated in type 1 pelitic lithologies (> 1 wt. %) than in the more carbonated type 2 (0.5-1 wt. %) and type 3-4 (< 0.5 wt. %) rocks. Most of the calcschists analyzed here contain less than 100 ppm of Sr (types 1, 2) but Sr reaches 180 ppm in carbonate-rich type 4.

The most pelitic type 1 and type 2 calcschists are generally the most concentrated in LREE (Ce > 100 ppm, Fig. 5c) while the lowest concentrations are found in type 4 calcschists (Ce < 25 ppm, Fig. 5c). Chondrite-normalized REE patterns (Fig. 5c) show similarly decreasing trends from LREE to HREE for all calcschists, with La/Yb ratios around 20 and negative Eu anomalies (except for the Bourget sample). These patterns compare well with those of Corsican calcschists metamorphosed around 500-550 °C and ~ 2.3 GPa reported by Piccoli et al. (2016). However, $Al_2O_3$-rich calcschists from the present study (types 1 to 3) are one order of magnitude richer in REE (Fig. 5c).

Compared to the calcschists described above, the mafic sample from the Bourget locality (Bg-mafic: metamorphosed pillow breccia) shows higher contents in FeO (up to 55 % in the ACF, Fig. 5a), MgO (~15 wt. %), $Na_2O$ (~3 wt. %; Table 2), $TiO_2$ (~2 wt. %; Fig. 5b) and enrichments in V, Cr, Co and Ni (Table 2), elements typically enriched in mafic rocks. Bg-mafic is depleted compared to calcschists in CaO (5 wt. %), HREE, and in most LILE such as Sr (~10 ppm) Rb, Ba, Cs and Pb (Fig. 5c; Table 2).

### Lawsonite composition

As major elements of the different lawsonite types are very similar (see tables 3, 4, 5, 6), we focused on the trace element contents. In the following, chemical maps (obtained by electron

362 microscopy) are presented next to corresponding extended trace element patterns from LA-ICP-MS spot
363 analyses for each lawsonite type.

364 *Univalent cations and white mica contamination*

365 Even though preservation of lawsonite crystals has been a prevalent criterion for selection before
366 laser ablation, and each lawsonite ablation pattern has been carefully inspected to detect contamination
367 from inclusions, contamination remains apparent. A strongly positive correlation between K content and
368 Na, Ba, Rb and Cs contents is observed (Sup. Mat. 3). These elements are classically enriched in white
369 mica, in substitution of K. Because lawsonite is generally devoid of K, these specific enrichments are
370 attributed to white mica contamination via minute inclusions in lawsonite (see also Whitney et al., 2020).
371 Therefore, interpretation of analytical results does not incorporate Na, K, Ba, Rb and Cs in the following.
372 It is also noteworthy that Li appears to show a positive correlation with K, yet much weaker than for
373 other univalent cations (Sup. Mat. 3). Significant white mica contamination appears limited to these
374 elements as no other correlation with K is observed.

375 *Lawsonite composition in host calcschists (LwsA)*

376 Five areas have been analyzed in a pelitic schist (sample Tpx-A1). They contain dark LwsA
377 crystals with hourglass zoning, easily recognized on Ti maps (Fig. 6a, c). Crystals may exhibit both
378 sides of the hourglass (Fig. 6c) or only one (Fig. 6a) due to their orientation. In chemical maps (Fig. 6a,
379 c), hourglass zoning is faintly observed for Ce, with enriched domains similar to Ti (blue spots 30-32
380 and 34-35 in C1; spots 13, 14, 16 and 18 in C4) whereas Al is slightly depleted in these domains (C1,
381 Fig. 6a). Ce also shows enrichment in angular sectors in the center of lawsonite crystals, again anti-
382 correlated to Al (Fig. 6a) but not linked to specific Ti enrichment (close to spots 37 and 29 in Fig. 6a,
383 close to spot 15 of Fig. 6c).

384 Ti-rich hourglass domains (blue dots 30-32 and 34-35; Fig. 6a, b) show the highest
385 concentrations in Ti, Zr and Hf and the lowest concentrations in Sr, Y and Mn. REE patterns also show
386 large variations, in terms of slope and absolute values, whether located within or without the Ti-enriched
387 domains. Even though barely seen on elemental maps (Fig. 6a, c), core to rim variations appear
388 superimposed to the hourglass domain, in particular in Ti-rich domains (e.g., blue curves 30-32 and 34-
389 35 in Fig. 6b, blue and green curves in Fig. 6d): LREE content decreases from core to rim, while HREE
390 values remain almost constant, which tends to flatten the REE pattern slope and generate spoon-shaped
391 patterns. Ti also tends to decrease from core to rim in the Ti-rich domain (Fig. 8a). In the crystal core
392 (spot 15 on Fig. 6c), the Ce-enriched Ti-depleted domain shows the highest U, Zr, Y, Hf, REE, Fe, Mn
393 and Cr contents.

The LwsA crystal investigated in the third area (Fig. 6e) shows intricate zoning as tentatively schematized (Fig. 6f). Overall, Ti and Sr maps (Fig. 6e) show a lawsonite core (spots 1 and 8) rimmed by Ti-enriched lawsonite, itself rimmed by a Ti-poor, Sr-rich lawsonite border (green and blue zones in Fig. 6f, respectively). In the lawsonite core, hourglass zoning is observed with two domains: Ti-enriched (spots 01 and 08) and Sr-enriched (depleted triangle-shaped domain immediately below). Additionally, the Ti-rich domain shows variable Ti content (Fig. 6e, f, g), the lowest contents in Zr, Hf and Ni, and low LREE contents (spots 01 and 08, Fig. 6g). The enclosing lawsonite (spots 2 to 9) is generally Ti-rich and Sr-poor, with much dispersion and patchy domains. LA-ICP-MS analyses in this zone (spots 02, 03, 07, 09) show variable LREE contents, but almost similar HREE contents, resulting in flattened and curved patterns like those observed earlier (Fig. 6b, d). The Sr-rich Ti-poor border (spots 10 and 12) rimming LwsA (Fig. 6f) is enriched in Y and HREE, showing spoon-shaped REE patterns (Fig. 6g).

*Lawsonite composition in quartz-rich veins (LwsB)*

Cream-colored LwsB crystals have more homogeneous composition than LwsA crystals. None of the investigated LwsB crystals displays hourglass zoning. Other zoning patterns have been identified in LwsB crystals (Fig. 7). The first Ti map (Fig. 7a) features angular Ti-rich domains in crystal cores (LA-ICP-MS spots 38 to 41) surrounded by Ti-depleted rims (spots 42 and 43, Fig. 7a, b). These differences are highlighted in the interpretative sketch and a second map for Ti and Sr (Fig. 7c); it is tempting to interpret these as successive generations of lawsonite. The Ti-poor crystals are enriched in U, Sr, Y and HREE compared to the Ti-rich crystals (Fig. 7b).

*Lawsonite composition in multiquartz aggregates (LwsA* & LwsB*)*

Compositions of LwsA* and LwsB* from multiquartz aggregate Tpx-AB5 from Triplex are provided in Supplementary material 4. LwsB* shows the same features as LwsB with Ti-rich cores (Sup. Mat. 4a) and Ti-depleted rims corresponding to high Sr contents (Sup. Mat. 4b). The composition and distribution of the other trace elements (Sup. Mat. 4b) compare also well with LwsB.

In the schistose fragments included in veins, dark LwsA* cores often show pale rims (Sup. Mat. 4d) enriched in Ti and Cr (Sup. Mat. 4c) but not in Ce (spots 2 to 5, Sup. Mat. 4c). LwsA* cores (spots 06 to 09) show heterogeneous and patchy Ti-zoning, they are generally enriched in most LILE (and HFSE to a lower extent) but depleted in Pb and Sr (Sup. Mat. 4e).

*Minor and trace elements in lawsonite types along the Strada dell'Assietta transect*

In situ lawsonite compositions (Fig. 8, normalized to C1 chondrite, McDonough and Sun, 1995) are provided in Table 7 for each lawsonite type and each locality.

Dark LwsA crystals in host calcschist from Triplex area (Tpx-A1, Fig. 8b) display high values for U, Th and REE. Most LILE (K, Cs, Rb, Ba, Pb, Sr) display large variations between samples, sharing high Pb and Sr contents (10 to 100 times chondritic values) but low contents in the other LILE (down to $10^{-3}$ chondritic values). The dispersion is much lower for Pb and Sr than for other LILE. High field strength elements (HFSE; Zr, Ti, Hf) are also hugely variable: Zr content varies over four orders of magnitude, Hf and Y over three, Ti over two. These lawsonite crystals show peculiar REE patterns, with marked enrichment in LREE content for some, leading to a four order of magnitude dispersion. HREE are also scattered but enriched between 10 and 1000 times the chondritic values. Two signatures appear: LREE-enriched LwsA with a negative slope from LREE to HREE (La/Yb ~ 100), and LwsA with flat to positive REE profiles, with an inflection point around Gd. Metallic elements (Fe, Mn, Cr and Ni) are generally low with considerably smaller dispersion.

LwsB in isolated quartz-bearing veins from Triplex (Tpx-B1, Fig. 8c; Tpx-B3, Fig. 8d) and Desertes (Ds-B3, Fig. 8a) shows very similar patterns for most elements. LwsB shows less dispersion than LwsA, except for LILE in Tpx-B1 (Fig. 8c) that compare well with those of LwsA (Fig. 8b). U and Th contents are either comparable to those in LwsA (Fig. 8a-d) or lower (between 10- and 200-times chondritic values in Tpx-B1). Pb contents are comparable to those of LwsA, and Sr is slightly higher in LwsB (up to 1000 times the chondritic values). For HFSE, Zr and Hf contents are lower than in LwsA ($10^{-1}$ to $10^{-2}$ chondritic values) while Ti is similar (1-10, Fig. 8c). However, LwsB from Desertes shows higher LILE and HFSE than those from Triplex (Fig. 8a, c, d). REE patterns of LwsB show a slightly negative slope from LREE to HREE, as commonly observed in lawsonite (see compilation of Whitney et al., 2020). These patterns are consistent with some of the LwsA patterns in the host calcschist (Fig. 8b). A small positive anomaly in Eu is observed in sample Tpx-B1 only (Fig. 8c). Metallic element contents in LwsB from Triplex are comparable to those in LwsA crystals, although Ni is systematically very low (Fig. 8c, d). The Desertes locality shows LwsB with the highest content in metallic elements (Fig. 8a).

LwsD crystals (Tpx-D1, Fig. 8e) show trace element patterns generally like those of LwsA and LwsA*, with somewhat higher Sr and Y values, reaching 2000 times chondritic values. LILE, U, Th and all metallic elements are as high as for LwsA* and LwsC in the multiquartz aggregate Tpx-AC4. Part of LwsD crystals show relatively flat patterns from LREE to MREE and an enrichment of HREE starting from Ho, resulting in La/Yb ~$10^{-2}$. These patterns are similar to some of LwsA* and LwsC in multiquartz aggregate Tpx-AC4. (Fig. 8g). The other half of LwsD crystals is comparable with the most REE-enriched LwsA crystals in host calcschist (Fig. 8b, e).

Lawsonite crystals in multiquartz aggregates (LwsA* and LwsB*) in Triplex (Tpx-AB5, Fig. 8f) and Assietta Pass (As-AB1, Fig. 8h) show compositions overall similar to those of LwsA and LwsB, respectively (Fig. 8b, c). LILE and HFSE contents are generally consistent with similar variability

between lawsonite types (LwsA* are comparable to LwsA and LwsB* to LwsB). Yet LwsA* and LwsC from multiquartz aggregate Tpx-AC4 (Fig. 8g) show higher LILE, U, Th and metallic elements (Cr in particular) than LwsA in host calcschist and LwsA* from other samples. REE patterns are more distinctive: LwsA* and LwsC from multiquartz aggregate Tpx-AC4 (Fig. 8g) show pronounced spoon-shaped REE patterns similar to some of LwsA in host calcschist, while LwsA* from sample Tpx-AB5 (Fig. 8f) displays flat REE patterns around 10 to 100 times chondritic values, with one crystal showing a spoon-shaped REE pattern. Most LwsB* crystals from Triplex and sample As-AB1 from Assietta Pass show REE patterns consistent with those of LwsB (Fig. 8a, b, d, h), i.e. with a slightly negative slope and slightly curved. However, in sample As-AB1 from the Assietta pass, LwsB* growing with ankerite (Fig. 8h) shows convex REE patterns (i.e., richer in MREE; Fig. 8h), which is also observed for a few LwsB* crystals from Triplex (Fig. 8f). In the multiquartz aggregate from the Assietta Pass, LwsC crystals show trace element patterns similar to those of neighboring LwsA* (Fig. 8i), with both spoon-shaped and convex REE patterns.

Overall, two key observations can be made in the context of expected lawsonite composition from the literature (Martin et al., 2014; Vitale Brovarone et al., 2014; Whitney et al., 2020; Kang et al., 2022). First, enrichment in some elements (LREE, U, Th, Pb, Sr) stands out, in particular for LwsA, LwsA* and LwsD crystals. Second, the dispersion of analyses is huge, even within samples.

### Lawsonite $^{87}Sr/^{86}Sr$ ratios

Comparing $^{87}Sr/^{86}Sr$ ratios from lawsonite crystals and corresponding whole rocks from each location reveals no viable isochron relationships (Fig. 9). To correct the isotopic ratios to the time of blueschist-facies metamorphism, the data were corrected by assuming lawsonite growth ages of 60, 50 or 40 Ma (Table 8). At first order, lawsonite separates display different signatures along the transect (Fig. 9a), varying between 0.7113 near the Piemont margin units (westward) and ratios around 0.7140 at the Assietta pass (eastward). Near the contact with the Piemont margin units, LwsA at Desertes shows similar $^{87}Sr/^{86}Sr$ ratios to LwsB collected on the same outcrop (DS02A). The sample collected at Fraiteve (Ft-D1) containing LwsD shows an $^{87}Sr/^{86}Sr$ ratio of 0.712635 (± 0.000013). At Triplex, where the lawsonite content is maximum (see Fig. 1d), all four LwsA samples show similar $^{87}Sr/^{86}Sr$ ratios (Table 8) around 0.7128, very close to the LwsC sample. The LwsB sample collected at Triplex shows higher $^{87}Sr/^{86}Sr$ ratios than LwsA and reaches 0.713708 (± 0.000015). LwsD contained in sample SL07B shows values higher to LwsB and reaches up to 0.714352 (± 0.000008). LwsA at Bourget has higher $^{87}Sr/^{86}Sr$ ratio than LwsA in Triplex. At the Assietta pass, LwsA and LwsB show comparable $^{87}Sr/^{86}Sr$ ratios around 0.7140.

Overall, $^{87}Sr/^{86}Sr$ ratios in lawsonite apparently increase eastward (Fig. 9a), though with significant local variability best demonstrated at Triplex, from 0.7112 at Desertes to .7138 at Assietta.

The $^{87}Sr/^{86}Sr$ ratios in lawsonite are not correlated with Sr and Rb concentrations (Fig. 9b-c) nor with $^{87}Rb/^{86}Sr$ ratio. In the bulk rocks, Sr isotopic ratios are inversely correlated to Sr concentration for the least radiogenic group, but not for the most radiogenic samples and the entire dataset appears scattered. Whole rock and lawsonite values are relatively close to each other at Fraiteve and Triplex (to the west) whereas whole rock and lawsonite values are markedly disparate at Bourget and Assietta (to the east).

# DISCUSSION AND GEOLOGICAL IMPLICATIONS

## Composition of lawsonite in calcschists

Lawsonite is increasingly suggested as a proxy for fluid/rock interactions during subduction through its geochemistry, as reviewed by Whitney et al. (2020) and Kang et al. (2022). However, metasedimentary lawsonite is less frequently observed in outcropping rocks and has not been much studied compared to metamafic lawsonite. Comparing the Fe and Al + Cr + Ti contents to the compilation of exhumed lawsonite worldwide (Fig. 10a; Kang et al., 2022) shows that calcschist lawsonite follows a specific trend, different from those identified by Kang et al. (2022). Here, calcschist lawsonite does not contain more than 0.04 Fe a.p.f.u. (regardless of the lawsonite type, Tables 3, 4, 5, 6) which may be linked to the incorporation of Fe in ankerite co-stable with lawsonite. The Pb and Sr contents have been used by Whitney et al. (2020) to classify lawsonite compositions, where Sr/Pb ratio below 40 are related to metasedimentary lawsonite (in Qz-rich metasediments, Kang et al., 2022); higher Sr/Pb ratios were interpreted as reflecting metamafic lawsonite (characterized by moderate Sr/Pb below 130 and high Sr/Pb for greater values). Most analyses of the Alpine SL lawsonite types fall in the moderate metamafic lawsonite field of Whitney et al. (2020; Fig. 10b) inconsistent with the lithology. Abundance of lawsonite in type 2 and type 3 lithologies of the SL is linked to the presence of carbonates involved in lawsonite crystallization. Here lawsonite compositional trends reflect local fluid-rock interactions rather than larger-scale fluid migrations.

## Distribution of trace elements in lawsonite types

Lawsonite easily incorporates trace elements into its structure owing to multiple potential substitutions on Al and Ca sites, the latter being easily deformed and therefore prone to hosting large cations (Ueno et al., 1999; Dubacq and Plunder, 2018). Itoigawaïte has been recognized as the Sr equivalent of lawsonite, where Sr occupies the Ca site (Miyajima et al., 1999), suggesting extensive solid solution between the two.

*Hourglass sector zoning*

Hourglass zoning, observed in LwsA only, dramatically affects Ti (Fig. 6a, c, e). Ti-rich domains also correspond to high LREE concentrations, as illustrated on Ce maps (Fig. 6a, c), to Zr and Hf enrichment (Figs. 6b, d, 10c) but correspond to Sr depletion (Figs. 6e, 10d). Preferential incorporation of Ti and LREE is commonly observed in metasedimentary lawsonite (Ueno et al., 1999; Martin et al., 2011, 2014; Vitale Brovarone et al., 2014), while Ti and Fe hourglass zoning are reported for lawsonite in mafic rocks (Fornash et al., 2019). Hourglass zoning is classically observed in magmatic clinopyroxene and metamorphic staurolite (e.g., Hollister, 1970; Hollister and Gancarz, 1971; Dowty, 1976) and appears restricted to specific mineral groups, including tourmaline (Van Hinsberg, 2006). Hourglass zoning is attributed to differential uptake of elements on crystal faces exposed to fluids (Van Hinsberg, 2006). Dowty (1976) showed that this preferential incorporation is controlled by the crystal structure: some elements show a higher affinity with some crystal faces due to electrostatic interactions, increasing their adsorption rate during growth. Fornash et al. (2019) identified potential correlations between the presence of subgrains and the shape of the hourglass zoning, potentially indicating that deformation processes might also play a key role in trace element partitioning while lawsonite crystallizes. Hourglass zoning has therefore been identified as an out-of-equilibrium feature, linked to rapid crystallization (Vitale Brovarone et al., 2014). Practically, crystals showing hourglass zoning provide support that equilibrium was not reached, at least for some elements, with the consequence that thermodynamic modeling and/or partition coefficients based on formula unit properties will fail at reproducing the incorporation of these trace elements in lawsonite.

*Concentric growth zoning*

In Ti-enriched domains, concentrations of Ti and LREE are not constant. LREE are observed to decrease from core to rim, resulting in flattened REE patterns (Fig. 6b, d). Ti also uniformly decreases from core to rim (Fig. 6c; patchy domains can be related to interface-coupled dissolution-precipitation, see below). These core-to-rim depletions, also observed in tourmaline by Van Hinsberg et al. (2006), are interpreted as reflecting a reservoir effect consistent with closed-system behavior, as for the classical Mn bell-shaped zoning in prograde garnet sometimes referred to as "garnet fractionation" (Tropper and Recheis, 2003; Kohn, 2005; Skora et al., 2006; Dubacq et al., 2019). Here concentric zoning is observed for immobile elements (large trivalent and quadrivalent cations) in lawsonite from pelitic parts, with the lowest permeability, after low-temperature crystallization (180 to 300°C). Assuming at least transient closed-system behavior is therefore reasonable, and backed by previous studies (Henry et al., 1996; Cook-Kollars et al., 2014; Lefeuvre et al., 2020; Herviou et al., 2021). The lack of systematics between cores and rims reflects the transient and local character, with homogenization over small length-scales in isolated parts of the schist. In other words, LwsA preferentially incorporates mobilized Ti and LREE to its hourglass domains, but these elements are probably not distributed homogeneously at any given

time in the surrounding schist over more than tens of centimeters, linked to the thickness of pelitic/carbonate alternations in the original sediment.

The combination of hourglass zoning and reservoir effects explains the dramatic variations in La/Yb ratios in LwsA crystals (Fig. 10e). Most of the available LREE are incorporated into Ti-enriched domains of LwsA while HREE contents remain homogeneous (Fig. 6b, d, g).

*Patchy zoning due to interface-coupled dissolution-precipitation*

A third feature observed on lawsonite chemical maps in the schistose lithologies (calcschists types 1 to 3 containing LwsA and/or LwsA*) relates to patchy zoning, consisting of enriched or depleted domains for some trace elements, and cross-cutting homogeneous or differently zoned domains for other elements. This is best seen on the Ti maps of LwsA* in Sup. Mat. 4c, f, where thin Ti-depleted domains are found together with hair-like Ti-enriched domains with a vague preferred orientation. Patchy Ti zoning is also observed for LwsA, either in the hourglass domain (Fig. 6c) or in overgrowths (Fig. 6e, f). Ce and Cr also show patchy or angular zoning in LwsA (Fig. 6a, c) and LwsA* (Sup. Mat. 4c, f). This contrast with hourglass zoning and concentric growth zoning in that the domains appear blurry and not linked to crystal axes. The domains cannot be attributed to contamination as depleted and enriched domains alternate (Figs. 6a, c, e). Interpretation of these patchy domains involves faster crystal growth than the homogenization rate of Ti (or Cr, Ce) in the fluid feeding the crystal at grain boundaries. This has been recognized as similar to interface-coupled dissolution-precipitation, a mechanism leading to spectacular zoning in many mineral groups (including carbonates, apatite, chloritoid, clinopyroxene and garnet) over all metamorphic grades (Martin, 2009; Martin et al. 2011; Ruiz-Agudo et al., 2014; Ague and Axler, 2016; Renard et al., 2019; Figowy et al., 2020). This mechanism is not observed in LwsB (grown from fluids in veins), where element mobility is likely much higher than in schistose lithologies and where crystals grew with much more open space, as the veins may represent incrementally opened structures (Lefeuvre et al., 2020; Herviou et al., 2023). Interface-coupled dissolution-precipitation may lead to zoning reflecting the distribution of immobile elements before crystallization of neoblasts, as suggested by Carlson (2002) and Martin (2009). Combined with sensitivity on element mobility, interface-coupled dissolution-precipitation will therefore lead to the decoupling of poorly mobile elements from one another (variably affected) and from more mobile elements (unaffected). Here, this translates as adding noise to correlations with Ti (Fig. 10c, d).

*Lawsonite overgrowths and system opening*

In the schist, LwsA shows overgrowths with distinct chemical fingerprints (Sr-enriched, Ti-depleted), as well as LwsB and LwsB* in HP veins and multiquartz aggregates (Figs. 6f, 7a, d, Sup. Mat. 4a). Overgrowths are Ti-depleted (Figs. 6e, 7a, d, Sup. Mat. 4a) but enriched in Sr, Y and HREE

(Figs. 6e, g, 7d) whether found in veins or in the schist. LREE contents in lawsonite overgrowths are variable but do not show clear systematic differences compared to cores (Figs. 6g, 7c, Sup. Mat. 4b).

Strontium-rich overgrowths (Fig. 7c) show that Sr is released in the fluid during lawsonite crystallization. Contrary to out-of-equilibrium element incorporation described above for LwsA cores, this likely reflects an increased length-scale for element transfer. Given that Sr is positively correlated with CaO in the bulk rocks and more concentrated in type 4 (carbonate-rich) calcschists (Fig. 2b) and considering that carbonates are the primary reservoir of Sr in these rock units, Sr-rich overgrowths may be interpreted as evidence of opening of the system to carbonates via fluids. Quantifying this requires modeling the origin and source of Sr in the rocks, for which bulk rock and lawsonite Sr isotopic signatures can yield constraints.

Strontium isotopic ratios for all samples (Fig. 9) are more radiogenic than expected from Cretaceous limestones (in the range 0.7073 – 0.7077; McArthur et al., 2001). The data from Triplex perhaps hint at inheritance from a Mesozoic protolith (139 ± 65 Ma; MSWD=160; Sup. Mat. 5) but this 'errorchron' age is far too old for Alpine HP metamorphism and lawsonite growth. Clearly these rocks failed to isotopically re-equilibrate at the local mineral scale during the Alpine metamorphism of these rocks which occurred around 40-60 Ma (e.g., Agard et al., 2002; Ghignone et al., 2021; Herviou and Bonnet, 2023; Gyomlai et al., 2023). Owing to the low temperatures of blueschist-facies metamorphism, this is not surprising. In bulk samples, the high Sr isotopic ratios are thought to reflect incorporation of terrestrial-derived sediments. This is motivated by the high Sr isotopic ratios of the ~300 to ~500 Ma crystalline basement from Massif Central, Piemont micro-continent and Adria, being eroded at the time of deposition of the SL: commonly in the range 0.703-0.715, ratios as high as 0.731 are reported (e.g. Talbert and Duthou, 1983; Duthou, 1984; Downes et al., 1990, 1991; von Raumer et al., 1999) and high Rb/Sr phases like micas deriving from these rocks could have even higher values. Non-metamorphic Upper Cretaceous sediments of the “nappe des Gets” and Helminthoid flysch, taken as approximate equivalents of the SL before subduction, contain variable and locally high amounts of terrigenous sediments, mostly in the form of clays but including plagioclase feldspar (Caron and Weidmann, 1967; Caron, 1972; Caron et al., 1981), a major host of Sr. Rock samples in the least radiogenic group (with $^{87}Sr/^{86}Sr$ ratios around 0.709) show decreasing isotopic ratios with Sr and Rb concentrations (Fig. 9b, c) possibly reflecting the rock pelitic/carbonate proportions. However, for the more radiogenic samples and the lawsonite separates, the absence of correlation between Sr content and isotopic ratio (Fig. 9b) is explained by the wide range of $^{87}Sr/^{86}Sr$ ratios in the pelitic fraction of the sediments: a unique mixing curve is not obtained because of the variability of the pelitic endmember. Incorporation of variable fractions of Hercynian basement-derived, variably radiogenic Sr into the rock and/or the lawsonite overgrowths leaves a blurry relationship between content and isotopic signature.

This small-scale variability of $^{87}Sr/^{86}Sr$ ratios and the lack of data on isotopic signatures for lawsonite cores vs rims precludes defining precisely the source of Sr feeding overgrowths. Therefore, Sr-rich overgrowths are proof of increased Sr mobility and consistent with limited system opening, but do not reflect increasing devolatilization of the limestones.

## Evolution of fluid circulation and element mobility length-scale in the Schistes Lustrés metasediments

Trace element distribution and zoning patterns in the different lawsonite types give insights into the evolution of element mobility and fluid circulation length-scales in the calcschists during burial (see Fig. 11).

LwsA (and LwsA*) in host calcschists appears first (Fig. 11a-b; Lefeuvre et al., 2020). Hourglass zoning indicates out-of-equilibrium incorporation for some trace elements, including Ti and LREE. Fine zoning in LREE and Ti shows small-scale migration of immobile elements via interface-coupled dissolution-precipitation. LREE core-to-rim depletion suggests progressive depletion in the surrounding fluid, explaining the high variability of trace element concentrations and the decreasing La/Yb ratios over time, correlating positively with Ti but negatively with Sr (Figs. 6e, f, 7d, 10d). This is consistent with a closed-system behavior and element transfer restricted to µm to mm scale. As LwsA starts crystallizing early during burial (predicted crystallization at ~0.4 GPa and 180°C; Lefeuvre et al., 2020), element mobility was likely restricted by the small amount of fluid available at grain boundaries and by sluggish diffusivity at such low temperature. The Sr-rich overgrowths in LwsA (Fig. 6e, f) are interpreted as recording a slightly more open-system behavior, with length-scales of element mobility reaching tens of centimeters (Fig. 11b). Increasing element mobility is likely due to the on-going dehydration reactions (mostly from the pelitic fraction, Lefeuvre et al., 2020), occurring until peak conditions (Fig. 11c, d). The similar Sr isotopic ratios of LwsA separates and bulk samples from Triplex also show evidence of local-scale element redistribution during LwsA crystallization.

The significance of the apparent eastward increase of Sr isotopic ratios in LwsA across the Strada dell'Assietta transect (Fig. 9a) remains unclear. However, metamorphic reactions occurring in the pelitic fraction with increasing P-T conditions, including destabilization and dehydration of clay minerals (see Vidal and Dubacq, 2009) and/or increasing dissolution of detrital plagioclase are likely to account for Sr isotopic changes. A denser sampling and further analyses on other phases (calcite and ankerite from the SL; plagioclase and clays from the Pre-Alps Gets unit, a non-metamorphic analog) are required to clarify this, as the evolution of the average Sr isotopic ratio of the detrital sediments during deposition is unknown. The large difference between lawsonite separates and whole rock $^{87}Sr/^{86}Sr$ for all locations east of Triplex is also an unresolved first-order problem. There, lawsonite separates are far more radiogenic than their host rocks, unlike locations further to the west. It is possible that the lawsonite

crystals grew from Rb-rich phases out-of-equilibrium with the rest of the whole rock (e.g., detrital micas and mica-like clay minerals), inheriting their elevated $^{87}Sr/^{86}Sr$. Alternatively, this could reflect open system influx of a radiogenic Sr rich fluid that was more significant in the east than in the west.

Although interpretations for LwsC and LwsD cannot be generalized due to a lack of data for these scarce lawsonite types, it is noteworthy that LwsC veins in multiquartz aggregate present mineral assemblages and trace element patterns similar to the neighboring LwsA* in the calcschists (Fig. 8g), and LwsD in the host rocks is very similar to LwsA and LwsA* (Fig. 8b, e, f). Therefore, LwsC and LwsD may have formed from the same local fluid, transferring elements only at the meter scale or smaller, restricted to the meter.

The elemental homogeneity of LwsB and LwsB* cores (Fig. 8a, c, d, f, h) suggests that the vein network collecting internally derived fluids allowed efficient homogenization and element redistribution. As for LwsA, Sr-rich overgrowths (LwsB2, Fig. 7b, c) likely reflect an increasing distance of element transfer during LwsB crystallization, in agreement with the incremental growth patterns of LwsB fibers (Lefeuvre et al., 2020). LwsB $^{87}Sr/^{86}Sr$ ratios are higher than those of LwsA at Triplex but lower at Desertes and similar at Assietta, which is also consistent with opening of the LwsB vein network to surrounding pelitic/carbonate layers with variable Sr isotopic ratios. LwsB and LwsB* show similar trace element patterns all along the Strada dell'Assietta transect, suggesting that similar small-scale processes acted synchronously along the transect, regardless of the varied pressure-temperature conditions. However, the heterogeneity of their Sr isotopic signature (Fig. 9) suggests that the scale of fluid homogenization in LwsB vein network did not reach the km-scale but was efficient on the order of hundreds of meters (sub-unit scale; Fig. 11c) in a transiently connected LwsB vein network, continually evolving with ductile deformation.

Overall, our results are in line with previous isotopic, trace elements and fluid inclusions studies suggesting a closed-system behavior with a limited scale of fluid circulation inside the SL units during subduction (Henry et al., 1996; Agard et al., 2000; Bebout et al., 2013; Cook-Kollars et al., 2014; Epstein et al., 2020; Herviou et al., 2021). This small scale and pervasive fluid circulation is also supported by the distribution of veins across outcrops (Herviou et al., 2023). However, a local and limited influx of fluid containing radiogenic Sr cannot be ruled out at Triplex and locations further east, where lawsonite separates show both the highest and most variable $^{87}Sr/^{86}Sr$ ratios, and where multiquartz aggregates are numerous.

During prograde and peak metamorphism, fluids are internally produced via dehydration reactions in pelitic horizons and react with carbonate layers (see also Herviou et al., 2021) but mobilized elements are rapidly trapped in lawsonite and newly formed carbonates. Growth of LwsA in the schist leads to rapid, effective immobilization of poorly mobile elements like Ti, in addition to consuming

693 water. Crystallization of lawsonite follows a continuum (see Lefeuvre et al., 2020) starting early in the
694 subduction history and lasting until peak metamorphic conditions (Fig. 11d). Along this continuum,
695 opening of the system appears progressive, with increasing fluid-rock interaction scales (from mm-scale
696 to m-scale, Fig. 11a-c.), as shown by i) incremental growth of LwsA, ii) appearance of other lawsonite
697 types in veins, iii) reaction fronts along the carbonate/pelite interfaces, with rock mixing and reaction
698 rates enhanced by deformation (Lefeuvre et al., 2020), and iv) isotopic disequilibrium of Sr between
699 lawsonite veins and the surrounding schist. Despite evidence for increasing fluid circulation and system
700 opening over time, no evidence for large-scale mass transfer, even close to tectonic contacts, is found.

701 The limited fluid flux inside the SL units compared to the larger fluid circulation suggested in tectonic
702 contacts and in lithological boundaries (e.g., Angiboust et al., 2014; Locatelli et al., 2019; Herviou and
703 Bonnet, 2023) explains the important differences in the geochemical behavior of elements during
704 crystallization of lawsonite from lawsonitite found in metasomatic aureoles (e.g., Piccoli et al., 2018;
705 Vitale Brovarone et al., 2020).

706 ## CONCLUSIONS

707 The upper units of the Schistes Lustrés deep accretionary complex show an intricate record of
708 extensive fluid/rock interactions in sediments metamorphosed at blueschist-facies conditions. In these
709 units, lawsonite is ubiquitous in veins and in the surrounding schists, crystallized from early prograde
710 to peak burial conditions. This study based on major, trace elements and Sr isotopic ratios provides a
711 detailed framework for petrological and geochemical interpretation of the complex geochemical record
712 of lawsonite. White mica contamination has been found to be difficult to avoid and hinders
713 interpretations based on content of univalent cations. For other minor and trace elements, this study
714 shows that several processes affected the composition of lawsonite, decoupling elements from one
715 another, mostly based on their mobility. These processes take place at equilibrium and out-of-
716 equilibrium, resulting in zoning, apparently unrelated to the changing pressure-temperature conditions.
717 At crystal scale, two main types of zoning are observed: hourglass zoning in the calcschists and growth
718 zoning both in the schists and in the veins. Hourglass zoning preferentially affects Ti and LREE.
719 Concentric growth zoning is best observed for Ti, REE, Hf and Zr, and likely involves many other
720 elements less dramatically. Combination of these mechanisms results in large variability of trace element
721 contents, especially REE that vary over four orders of magnitude. Over time during prograde
722 metamorphism, the La/Yb ratio decreases strongly (from ~100 to ~1) as La appears much more sensitive
723 than Yb to crystal surface effects leading to hourglass zoning.

724 Interface-coupled dissolution-precipitation is a third mechanism decoupling elements in the
725 calcschists and involving poorly mobile elements. It is again best observed for Ti, but affects REE and
726 Cr too, resulting in poor correlations between elements.

Lastly, overgrowths, best observed in varying Sr content, show system opening in the veins. System opening remains limited in the host calcschists. Sr isotopic ratios that are consistently more radiogenic than the marine carbonate protolith rule out limestone devolatilization as the main driver of fluid flow and source of the Sr. The overall mineral compositional evolution records progressive and incremental system opening, first limited to tens of centimeters, then to the subunit scale, at the order of hundreds of meters at most. Large-scale mass transfer and fluid influx from external sources are not supported even though the vein network extends over time until peak conditions. This vein network appears fed by internal fluids and enhanced by deformation. In the schists, transfer via fluid advection was limited to mobile elements like Sr during the last growth increments. Comparison between the composition of lawsonite in veins and in the schist has been found critical for interpretation of varying fluid composition over space and time.

## Acknowledgments

This work was financially supported by the SYSTER program of CNRS-INSU, by ISTeP and by the ZIP project (REA grant agreement no. 604713 (ZIP "Zooming In between Plates") from the People Program (Marie Curie Actions) of the European Union's Seventh Framework Program FP7/2007-2013) as well as National Science Foundation Grant PIRE-1545903. We thank O. Boudouma and D. Deldique for their expertise with SEM characterization; M. Fialin and N. Rividi for help with EPMA; B. Villemant and J. Noel for ICP-OES and LA-ICP-MS measurements; E. Delairis for making the thin and thick sections. We also thank H. Raimbourg, L. Jolivet, L. Martin, A. Vitale Brovarone, M. Ballèvre and M. Feineman for insightful discussions during the PhD defense of the first author. Detailed and constructive reviews and comments by three anonymous reviewers and the editor O. Müntener are gratefully acknowledged.

## REFERENCES

Agard, P. (2021). Subduction of oceanic lithosphere in the Alps: Selective and archetypal from (slow-spreading) oceans. Earth-Science Reviews, 103517.

Agard, P., Goffé, B., Touret, J.L.R., Vidal, O., 2000. Retrograde mineral and fluid evolution in high-pressure metapelites (Schistes lustrés unit, Western Alps). Contributions to Mineralogy and Petrology 140, 296–315.

Agard, P., Jolivet, L., Goffé, B. (2001). Tectonometamorphic evolution of the Schistes Lustrés complex: implications for the exhumation of HP and UHP rocks in the western Alps. Bulletin de la Société Géologique de France 172, 617–636.

Agard, P., Monié, P., Jolivet, L., Goffé, B. (2002). Exhumation of the Schistes Lustrés complex: in situ laser probe 40Ar/39Ar constraints and implications for the Western Alps. Journal of metamorphic Geology 20, 599–618.

Agard, P., Yamato, P., Jolivet, L., Burov, E., (2009). Exhumation of oceanic blueschists and eclogites in subduction zones: Timing and mechanisms. Earth-Science Reviews 92, 53–79. https://doi.org/10.1016/j.earscirev.2008.11.002

Agard, P., Plunder, A., Angiboust, S., Bonnet, G., Ruh, J., (2018). The subduction plate interface: rock record and mechanical coupling (from long to short timescales). Lithos 320–321, 537–566. https://doi.org/10.1016/j.lithos.2018.09.029

Agard, P., & Handy, M. R. (2021). Ocean subduction dynamics in the Alps. Elements 17, 9–16.

Ague, J.J., Axler, J.A. (2016). Interface coupled dissolution-reprecipitation in garnet from subducted granulites and ultrahigh-pressure rocks revealed by phosphorous, sodium, and titanium zonation. American Mineralogist 101, 1696–1699. https://doi.org/10.2138/am-2016-5707

Ague, J. J., & Nicolescu, S. (2014). Carbon dioxide released from subduction zones by fluid-mediated reactions. Nature Geoscience, 7(5), 355-360.

Angiboust, S., Langdon, R., Agard, P., Waters, D., Chopin, C., (2012). Eclogitization of the Monviso ophiolite (W. Alps) and implications on subduction dynamics. Journal of Metamorphic Geology 30, 37–61. https://doi.org/10.1111/j.1525-1314.2011.00951.x

Angiboust, S., Pettke, T., De Hoog, J. C., Caron, B., & Oncken, O. (2014). Channelized fluid flow and eclogite-facies metasomatism along the subduction shear zone. Journal of petrology, 55(5), 883-916.

Baxter E.F., and Caddick, M.J., 2013. Garnet growth as a proxy for progressive subduction zone dehydration. Geology, 41, 643-646.

Bebout, G.E., Agard, P., Kobayashi, K., Moriguti, T., Nakamura, E. (2013). Devolatilization history and trace element mobility in deeply subducted sedimentary rocks: Evidence from Western Alps HP/UHP suites. Chemical Geology 342, 1–20. https://doi.org/10.1016/j.chemgeo.2013.01.009

Beyssac, O., Goffé, B., Chopin, C., Rouzaud, J.N. (2002). Raman spectra of carbonaceous material in metasediments: a new geothermometer. Journal of metamorphic Geology 20, 859–871.

Carlson, W. D. (2002) Scales of disequilibrium and rates of equilibration during metamorphism American Mineralogist, 87, 185 DOI: 10.2138/am-2002-2-301

Caron, J.M. (1974). Rapports entre diverses “générations” de lawsonite et les déformations dans les Schistes lustrés des Alpes cottiennes septentrionales (France et Italie). Bulletin de la Société Géologique de France 255–263.

Caron, C., & Weidmann, M. (1967). Sur les flysch de la région des Gets (Haute-Savoie). Birkhäuser.

Caron, C. (1972). La Nappe Supérieure des Préalpes: subdivisions et principaux caractères du sommet de l'édifice préalpin.

Caron, C., Hesse, R., Kerckhove, C., Homewood, P., Van Stuijvenberg, J., Tasse, N., & Winkler, W. (1981). Comparaison préliminaire des flyschs à Helminthoïdes sur trois transversales des Alpes. Eclogae Geologicae Helvetiae, 74, 369-378.

790 Cook-Kollars, J., Bebout, G.E., Collins, N.C., Angiboust, S., Agard, P. (2014). Subduction zone metamorphic pathway for
791 deep carbon cycling: I. Evidence from HP/UHP metasedimentary rocks, Italian Alps. Chemical Geology 386, 31–
792 48. https://doi.org/10.1016/j.chemgeo.2014.07.013

793 Coward, M., Dietrich, D. (1989). An overview– Alpine tectonics. Geological Society, London, Special Publications 45.

794 Deville, E, (1986). La klippe de la Pointe du Grand Vallon (Vanoise-Alpes occidentales) : un lambeau de métasédiments à
795 foraminifères du Maastrichtien supérieur couronnant les nappes de « schistes lustrés ». Comptes rendus de
796 l'Académie des sciences. Série 2, Mécanique, Physique, Chimie, Sciences de l'univers, Sciences de la Terre 303,
797 1221–1226.

798 Deville, E., Fudral, S., Lagabrielle, Y., Marthaler, M., Sartori, M. (1992). From oceanic closure to continental collision: A
799 synthesis of the" Schistes lustrés" metamorphic complex of the Western Alps. Geological Society of America Bulletin
800 104, 127–139.

801 De Wever, P., & Caby, R. (1981). Datation de la base des schistes lustrés postophiolitiques par des radiolaires (Oxfordien-
802 Kimmeridgien moyen) dans les Alpes Cottiennes (Saint Véran, France). Compte rendu de l'académie des Sciences
803 de Paris, 292, 467-472.

804 Downes, H., Dupuy, C., & Leyreloup, A. F. (1990). Crustal evolution of the Hercynian belt of Western Europe: Evidence from
805 lower-crustal granulitic xenoliths (French Massif Central). Chemical Geology, 83(3-4), 209-231.

806 Downes, H., Bodinier, J. L., Thirlwall, M. F., Lorand, J. P., & Fabries, J. (1991). REE and Sr-Nd isotopic geochemistry of
807 eastern Pyrenean peridotite massifs: sub-continental lithospheric mantle modified by continental magmatism. Journal
808 of Petrology, (2), 97-115.

809 Dowty, E. (1976). Crystal structure and crystal growth: II. Sector zoning in minerals. American Mineralogist 61, 460–469.

810 Dubacq, B., Soret, M., Jewison, E., Agard, P. (2019). Early subduction dynamics recorded by the metamorphic sole of the Mt.
811 Albert ophiolitic complex (Gaspé, Quebec). Lithos 334–335, 161–179. https://doi.org/10.1016/j.lithos.2019.03.019

812 Dubacq, B., & Plunder, A. (2018). Controls on trace element distribution in oxides and silicates. Journal of Petrology, 59(2),
813 233-256.

814 Duthou, J. L. (1984). Age dévonien supérieur (Rb/Sr) des gneiss acordiérite de la carriere du Puy-du-Roi aAubusson
815 (Creuse). Consé quences. 10e Ré un. ann. sci. Terre, Bordeaux.

816 Enami, M. (1999). CaAl-silicates: an important Sr container in subducted slab. Journal of Geography (Chigaku Zasshi), 108(2),
817 177-187.

818 Epstein, G.S., Bebout, G.E., Angiboust, S., Agard, P. (2020). Scales of Fluid-Rock Interaction and Carbon Mobility in the
819 Deeply Underplated and HP-Metamorphosed Schistes Lustrés, Western Alps. Lithos 105229.
820 https://doi.org/10.1016/j.lithos.2019.105229

821 Figowy, S., Dubacq, B., Noël, Y., & d'Arco, P. (2020). Partitioning of chromium between garnet and clinopyroxene: first-
822 principle modelling versus metamorphic assemblages. European Journal of Mineralogy, 32(4), 387-403.

Fornash, K.F., Whitney, D.L., Seaton, N.C.A. (2019). Lawsonite composition and zoning as an archive of metamorphic processes in subduction zones. Geosphere. https://doi.org/10.1130/GES01455.1

Fudral, S. (1996). Etude géologique de la suture tethysienne dans les Alpes franco-italiennes Nord-Occidentales de la Doire Ripaire (Italie) à la région de Bourg Saint-Maurice. (France) (Doctoral dissertation, Université de Savoie).

Gabalda, S., Beyssac, O., Jolivet, L., Agard, P., & Chopin, C. (2009). Thermal structure of a fossil subduction wedge in the Western Alps. Terra Nova, 21(1), 28-34.

Ghignone, S., Gattiglio, M., Balestro, G., & Borghi, A. (2020). Geology of the Susa Shear Zone (Susa Valley, Western Alps). Journal of Maps, 16(2), 79-86.

Ghignone, S., Borghi, A., Balestro, G., Castelli, D., Gattiglio, M., & Groppo, C. (2021). HP tectono-metamorphic evolution of the Internal Piedmont Zone in Susa Valley (Western Alps): New petrologic insight from garnet+ chloritoid-bearing micaschists and Fe–Ti metagabbro. Journal of Metamorphic Geology, 39(4), 391-416.

Gyomlai, T., Yamato, P., & Godard, G. (2023). Petrological study of an eclogite-facies metagranite from the Champtoceaux Complex (La Picherais, Armorican Massif, France). European Journal of Mineralogy, 35(4), 589-611.

Hacker, B.R., Abers, G.A. (2004). Subduction Factory 3: An Excel worksheet and macro for calculating the densities, seismic wave speeds, and H2O contents of minerals and rocks at pressure and temperature. Geochemistry, Geophysics, Geosystems 5, n/a-n/a. https://doi.org/10.1029/2003GC000614

Hacker, B.R., Peacock, S.M., Abers, G.A., Holloway, S.D. (2003). Subduction factory 2. Are intermediate-depth earthquakes in subducting slabs linked to metamorphic dehydration reactions? Journal of Geophysical Research: Solid Earth 108. https://doi.org/10.1029/2001JB001129

Handy, M.R., M. Schmid, S., Bousquet, R., Kissling, E., Bernoulli, D. (2010). Reconciling plate-tectonic reconstructions of Alpine Tethys with the geological–geophysical record of spreading and subduction in the Alps. Earth-Science Reviews 102, 121–158. https://doi.org/10.1016/j.earscirev.2010.06.002

Hara, T., Tsujimori, T., Chang, Q., & Kimura, J. I. (2018). In-situ Sr-Pb isotope geochemistry of lawsonite: A new method to investigate slab-fluids. Lithos, 320, 93-104.

Hara, T., Tsujimori, T., Flores, K. E., & KIMURA, J. I. (2019). Sr–Pb isotope compositions of lawsonites in a Pacheco Pass metagraywacke, Franciscan Complex, California. Journal of Mineralogical and Petrological Sciences, 114(6), 296-301.

Henry, C., Burkhard, M., Goffé, B. (1996). Evolution of synmetamorphic veins and their wallrocks through a Western Alps transect: no evidence for large-scale fluid flow. Stable isotope, major- and trace-element systematics. Chemical Geology 127, 81–109. https://doi.org/10.1016/0009-2541(95)00106-9

Herviou, C., Verlaguet, A., Agard, P., Locatelli, M., Raimbourg, H., Lefeuvre, B., & Dubacq, B. (2021). Along-dip variations of subduction fluids: The 30–80 km depth traverse of the Schistes Lustrés complex (Queyras-Monviso, W. Alps). Lithos, 394, 106168.

Herviou, C., Agard, P., Plunder, A., Mendes, K., Verlaguet, A., Deldicque, D., & Cubas, N. (2022). Subducted fragments of the Liguro-Piemont ocean, Western Alps: Spatial correlations and offscraping mechanisms during subduction. Tectonophysics, 827, 229267.

Herviou, C., & Bonnet, G. (2023). Paleocene-Eocene High-Pressure Carbonation of Western Alps Serpentinites: Positive Feedback Between Deformation and CO2-CH4 Fluid Ingression Responsible for Slab Slicing? Geochemistry, Geophysics, Geosystems, 24(3), e2022GC010557.

Herviou, C., Agard, P., Verlaguet, A., Gyomlai, T., Bonnet, G., Mendes, K., & Plunder, A. (2023). Fractal Distribution of Subduction-Related Crack-Seal Veins (Schistes Lustrés, W. Alps): Implications for Fluid Flow and Rupture Processes at the Downdip End of the Seismogenic Zone. Journal of Geophysical Research: Solid Earth, 128(10).

Hollister, L.S. (1970). Origin; mechanism, and consequences of compositional sector-zoning in staurolite. The American mineralogist 55, 742–766.

Hollister, L.S., Gancarz, A.J. (1971). Compositional sector-zoning in clinopyroxene from the Narce area, Italy. The American mineralogist 56, 959–979.

Jaeckel, K., Bebout, G.E., Angiboust, S. (2018). Deformation-enhanced fluid and mass transfer along Western and Central Alps paleo-subduction interfaces: Significance for carbon cycling models. Geosphere 14, 2355–2375. https://doi.org/10.1130/GES01587.1

Kang, P., Whitney, D. L., Martin, L. A., & Fornash, K. F. (2022). Trace and rare earth element compositions of lawsonite as a chemical tracer of metamorphic processes in subduction zones. Journal of Petrology, 63(8), egac065.

Kleine, B. I., Skelton, A. D., Huet, B., & Pitcairn, I. K. (2014). Preservation of blueschist-facies minerals along a shear zone by coupled metasomatism and fast-flowing CO2-bearing fluids. Journal of Petrology, 55(10), 1905-1939.

Kohn, M.J. (2005). Geochemical zoning in metamorphic minerals. In: Holland, H.D., Turekian, K.K. (Eds.), Treatise on Geochemistry. Pergamon, Oxford, pp. 229–261.

Lagabrielle, Y., (1987). Les ophiolites: Marqueurs de l'histoire tectonique des domaines océaniques. PhD thesis Brest.

Lagabrielle, Y., Cannat, M. (1990). Alpine Jurassic ophiolites resemble the modern central Atlantic basement. Geology 18, 319–322.

Lagabrielle, Y., Lemoine, M. (1997). Alpine, Corsican and Apennine ophiolites: the slow-spreading ridge model. Comptes Rendus de l'Académie des Sciences-Series IIA-Earth and Planetary Science 325, 909–920.

Lagabrielle, Y., Vitale Brovarone, A., Ildefonse, B., (2015). Fossil oceanic core complexes recognized in the blueschist metaophiolites of Western Alps and Corsica. Earth-Science Reviews 141, 1–26. https://doi.org/10.1016/j.earscirev.2014.11.004

Lapen, T.J., Johnson, C.M., Baumgartner, L.P., Mahlen, N.J., Beard, B.L., Amato, J.M. (2003). Burial rates during prograde metamorphism of an ultra-high-pressure terrane: an example from Lago di Cignana, western Alps, Italy. Earth and Planetary Science Letters 215, 57–72. https://doi.org/10.1016/S0012-821X (03)00455-2

889 Le Pichon, X., Bergerat, F., Roulet, M.-J. (1988). Plate kinematics and tectonics leading to the Alpine belt formation; a new
890 analysis. Geological Society of America Special Papers 218, 111–132.

891 Lefeuvre B. (2020). La lawsonite dans les métasédiments en base de zone sismogénique: géochimie, échelles de migration des
892 fluides et rôle de la déformation dans les Schistes Lustrés (Doctoral dissertation, Sorbonne université, Paris).

893 Lefeuvre, B., Agard, P., Verlaguet, A., Dubacq, B., Plunder, A. (2020). Massive formation of lawsonite in subducted sediments
894 from the Schistes Lustrés (W. Alps): Implications for mass transfer and decarbonation in cold subduction zones.
895 Lithos 105629. https://doi.org/10.1016/j.lithos.2020.105629

896 Lemoine, M., (2003). Schistes lustrés from Corsica to Hungary: back to the original sediments and tentative dating of partly
897 azoic metasediments. Bulletin de la Société Géologique de France 174, 197–209. https://doi.org/10.2113/174.3.197

898 Lemoine, M., Marthaler, M., Caron, M., Sartori, M., Amaudric du Chaffaut, S., (1984). Découverte de foraminifères
899 planctoniques du Crétacé supérieur dans les schistes lustrés du Queyras (Alpes occidentales). Conséquences
900 paléogéographiques et tectoniques. Comptes-rendus des séances de l'Académie des sciences. Série 2, Mécanique-
901 physique, chimie, sciences de l'univers, sciences de la terre 299, 727–732.

902 Lemoine, M., Tricart, P., (1986). Les Schistes lustrés piémontais des Alpes Occidentales : approche stratigraphique, structurales
903 et sédimentologique. Eclogae Geologicae Helvetiae 79, 271–294. https://doi.org/10.5169/SEALS-165835

904 Locatelli, M., Federico, L., Agard, P., & Verlaguet, A. (2019). Geology of the southern Monviso metaophiolite complex (W-
905 Alps, Italy). Journal of Maps, 15(2), 283-297.

906 Locatelli, M., Verlaguet, A., Agard, P., Federico, L., & Angiboust, S. (2018). Intermediate-depth brecciation along the
907 subduction plate interface (Monviso eclogite, W. Alps). Lithos, 320, 378-402.

908 Manzotti, P., Ballèvre, M., Pitra, P., & Schiavi, F. (2021). Missing lawsonite and aragonite found: P–T and fluid composition
909 in meta-marls from the Combin Zone (Western Alps). Contributions to Mineralogy and Petrology, 176(8), 1-27.

910 Marthaler, M., Stampfli, G.M., (1989). Les Schistes lustrés à ophiolites de la nappe du Tsaté : un ancien prisme d'accrétion de
911 la marge active apulienne ? Schweizerische Mineralogische und Petrographische Mitteilunge 69, 211–216.
912 https://doi.org/10.5169/SEALS-52789

913 Martin, L.A.J. (2009). Sub-millimeter heterogeneity of yttrium and chromium during growth of semi-pelitic garnet. Journal of
914 Petrology, 50(9), 1713-1727.

915 Martin, L.A.J., Hermann, J., Gauthiez-Putallaz, L., Whitney, D.L., Vitale Brovarone, A., Fornash, K.F., Evans, N.J. (2014).
916 Lawsonite geochemistry and stability - implication for trace element and water cycles in subduction zones. Journal
917 of Metamorphic Geology 32, 455–478. https://doi.org/10.1111/jmg.12093

918 Martin, L.A.J., Wood, B.J., Turner, S., Rushmer, T. (2011). Experimental Measurements of Trace Element Partitioning
919 Between Lawsonite, Zoisite and Fluid and their Implication for the Composition of Arc Magmas. Journal of Petrology
920 52, 1049–1075. https://doi.org/10.1093/petrology/egr018

McArthur, J. M., Howarth, R. J., & Bailey, T. R. (2001). Strontium isotope stratigraphy: LOWESS version 3: best fit to the marine Sr-isotope curve for 0–509 Ma and accompanying look-up table for deriving numerical age. The Journal of Geology, 109(2), 155-170.

McDonough, W.F., Sun, S. (1995). The composition of the Earth. Chemical Geology 223–253.

Mendes, K., Agard, P., Plunder, A., & Herviou, C. (2023). Lithospheric-scale dynamics during continental subduction: Evidence from a frozen-in plate interface. Geology, 51(12), 1153-1157.

Miyajima, H., Matsubara, S., Miyawaki, R., Ito, K. (1999). Itoigawaite, a new mineral, the Sr analogue of lawsonite, in jadeitite from the Itoigawa-Ohmi district, central Japan. Mineralogical Magazine 63, 909–916.

Nitsch, K.-H. (1972). Das P-T-XCO2 Stabilitätsfeld von Lawsonit. Contributions to Mineralogy and Petrology 34, 116–134.

Okamoto, K., Maruyama, S. (1999). The high-pressure synthesis of lawsonite in the MORB+ H2O system. American Mineralogist 84, 362–373.

Piccoli, F., Vitale Brovarone, A., Beyssac, O., Martinez, I., Ague, J.J., Chaduteau, C. (2016). Carbonation by fluid–rock interactions at high-pressure conditions: Implications for carbon cycling in subduction zones. Earth and Planetary Science Letters 445, 146–159. https://doi.org/10.1016/j.epsl.2016.03.045

Piccoli, F.; Vitale Brovarone, A. & Ague, J. J. (2018). Field and petrological study of metasomatism and high-pressure carbonation from lawsonite eclogite-facies terrains, Alpine Corsica. Lithos, 2018, 304-307, 16 - 37

Piccoli, F., Ague, J. J., Chu, X., Tian, M., & Vitale Brovarone, A. (2021). Field-based evidence for intra-slab high-permeability channel formation at eclogite-facies conditions during subduction. Geochemistry, geophysics, geosystems, 22(3), e2020GC009520.

Plank T. (2014). The chemical composition of subducting sediments. In:Rudnick RL (Ed.) The Crust. Treatise on Geochemistry. Elsevier, Oxford, pp. 607–629

Plank, T., Langmuir, C.H. (1998). The chemical composition of subducting sediment and its consequences for the crust and mantle. Chemical Geology 145, 325–394.

Platt, J.P., (1986). Dynamics of orogenic wedges and the uplift of high-pressure metamorphic rocks. Geol Soc America Bull 97, 1037–1053. https://doi.org/10.1130/0016-7606(1986)97<1037:DOOWAT>2.0.CO;2

Plunder, A., Agard, P., Dubacq, B., Chopin, C., Bellanger, M. (2012). How continuous and precise is the record of P-T paths? Insights from combined thermobarometry and thermodynamic modelling into subduction dynamics (Schistes Lustrés, W. Alps). Journal of Metamorphic Geology 30, 323–346. https://doi.org/10.1111/j.1525-1314.2011.00969.x

Polino, R. (1984). Les séries océaniques du Haut val de Suse (Alpes Cottiennes): analyse des couvertures sédimentaires. Ofioliti, 9, 547-554.

Polino, R, Dela Pierre, F, Borghi, A, Carraro, F, Fioraso, G, Giardino, M, (2002). Note illustrative della carta geologica d'Italia alla scala 1:50000: foglio 132-152-153 Bardonecchia. ISPRA, Servizio Geologico d'Italia.

953 Pouchou, J. L., & Pichoir, F. (1991). Quantitative analysis of homogeneous or stratified microvolumes applying the model
954 "PAP". Electron probe quantitation, 31-75.

955 Raimbourg, H., Famin, V., Palazzin, G., Mayoux, M., Jolivet, L., Ramboz, C., Yamaguchi, A., (2018). Fluid properties and
956 dynamics along the seismogenic plate interface. Geosphere 14, 469–491. https://doi.org/10.1130/GES01504.1

957 Renard, F., Røyne, A., Putnis, C.V. (2019). Timescales of interface-coupled dissolution-precipitation reactions on carbonates.
958 Geoscience Frontiers 10, 17–27. https://doi.org/10.1016/j.gsf.2018.02.013

959 Rice, A. H. N. & Mitchell, J. I. (1991). Porphyroblast textural sector-zoning and matrix displacement. Mineralogical Magazine,
960 Mineralogical Society, 55, 379-396 DOI: 10.1180/minmag.1991.055.380.08

961 Rosenbaum, G., Lister, G.S. (2005). The Western Alps from the Jurassic to Oligocene: spatio-temporal constraints and
962 evolutionary reconstructions. Earth-Science Reviews 69, 281–306. https://doi.org/10.1016/j.earscirev.2004.10.001

963 Ruiz-Agudo, E., Putnis, C.V., Putnis, A. (2014). Coupled dissolution and precipitation at mineral–fluid interfaces. Chemical
964 Geology 383, 132–146. https://doi.org/10.1016/j.chemgeo.2014.06.007

965 Schmid, S. M., Kissling, E., Diehl, T., van Hinsbergen, D. J., & Molli, G. (2017). Ivrea mantle wedge, arc of the Western Alps,
966 and kinematic evolution of the Alps–Apennines orogenic system. Swiss Journal of Geosciences, 110(2), 581-612.

967 Schmidt, M.W., Poli, S. (1998). Experimentally based water budgets for dehydrating slabs and consequences for arc magma
968 generation. Earth and Planetary Science Letters 163, 361–379. https://doi.org/10.1016/S0012-821X (98)00142-3

969 Schmidt, M.W., Poli, S. (1994). The stability of lawsonite and zoisite at high pressures: Experiments in CASH to 92 kbar and
970 implications for the presence of hydrous phases in subducted lithosphere. Earth and Planetary Science Letters 124,
971 105–118. https://doi.org/10.1016/0012-821X (94)00080-8

972 Schwartz, S., Guillot, S., Reynard, B., Lafay, R., Debret, B., Nicollet, C., Lanari, P., Auzende, A.L., (2013). Pressure–
973 temperature estimates of the lizardite/antigorite transition in high pressure serpentinites. Lithos 178, 197–210.
974 https://doi.org/10.1016/j.lithos.2012.11.023

975 Sicard-Lochon, E., & Potdevin, J. L. (1986). Transfert de matière à l'échelle de pseudomorphoses de lawsonite. Réunion
976 annuelle des sciences de la terre, 11.

977 Skora, S., Baumgartner, L. P., Mahlen, N. J., Johnson, C. M., Pilet, S., & Hellebrand, E. (2006). Diffusion-limited REE uptake
978 by eclogite garnets and its consequences for Lu–Hf and Sm–Nd geochronology. Contributions to Mineralogy and
979 Petrology, 152(6), 703-720.

980 Spandler, C., Hermann, J., Arculus, R., & Mavrogenes, J. (2003). Redistribution of trace elements during prograde
981 metamorphism from lawsonite blueschist to eclogite facies; implications for deep subduction-zone
982 processes. Contributions to Mineralogy and Petrology, 146, 205-222.

983 Stampfli, G. M., Mosar, J., Marquer, D., Marchant, R., Baudin, T., & Borel, G. (1998). Subduction and obduction processes in
984 the Swiss Alps. Tectonophysics, 296(1-2), 159-204.

985 Talbert, J., & Duthou, J. (1983). Upper carboniferous age (rb-sr) of the meymac granite (french massif central). Comptes rendus
986 de l'academie des sciences serie ii, 296(17), 1321-1323.

987 Tribuzio, R., Messiga, B., Vannucci, R., & Bottazzi, P. (1996). Rare earth element redistribution during high-pressure–low-
988 temperature metamorphism in ophiolitic Fe-gabbros (Liguria, northwestern Italy): Implications for light REE
989 mobility in subduction zones. Geology, 24(8), 711-714.

990 Tricart, P., Schwartz, S. (2006). A north-south section across the Queyras Schistes lustrés (Piedmont zone, Western Alps): Syn-
991 collision refolding of a subduction wedge. Eclogae Geologicae Helvetiae 99, 429–442.
992 https://doi.org/10.1007/s00015-006-1197-6

993 Tropper, P., & Recheis, A. (2003). Garnet zoning as a window into the metamorphic evolution of a crystalline complex: the
994 northern and central Austroalpine Ötztal-Complex as a polymorphic example. Mitteilungen der Österreichischen
995 Geologischen Gesellschaft, 94, 27-53.

996 Tsujimori, T., Sisson, V., Liou, J., Harlow, G., Sorensen, S. (2006). Very-low-temperature record of the subduction process: A
997 review of worldwide lawsonite eclogites. Lithos 92, 609–624. https://doi.org/10.1016/j.lithos.2006.03.054

998 Ueno, T. (1999). REE-bearing sector-zoned lawsonite in the Sanbagawa pelitic schists of the eastern Kii Peninsula, central
999 Japan. European Journal of Mineralogy 11, 993–998.

1000 Van Hinsberg, V.J. (2006). Hourglass sector zoning in metamorphic tourmaline and resultant major and trace-element
1001 fractionation. American Mineralogist 91, 717–728. https://doi.org/10.2138/am.2006.1920

1002 Van Keken, P.E., Hacker, B.R., Syracuse, E.M., Abers, G.A. (2011). Subduction factory: 4. Depth-dependent flux of H2O from
1003 subducting slabs worldwide. Journal of Geophysical Research 116. https://doi.org/10.1029/2010JB007922

1004 Vidal O., Dubacq B. (2009) Thermodynamic modelling of clay dehydration, stability and compositional evolution with
1005 temperature, pressure and H2O activity. Geochimica et Cosmochimica Acta 73, 6544 – 6564,
1006 doi: 10.1016/j.gca.2009.07.035

1007 Vitale Brovarone, A., Alard, O., Beyssac, O., Martin, L., Picatto, M. (2014). Lawsonite metasomatism and trace element
1008 recycling in subduction zones. Journal of Metamorphic Geology 32, 489–514. https://doi.org/10.1111/jmg.12074

1009 Vitale Brovarone, A., Beyssac, O. (2014). Lawsonite metasomatism: A new route for water to the deep Earth. Earth and
1010 Planetary Science Letters 393, 275–284. https://doi.org/10.1016/j.epsl.2014.03.001

1011 Vitale Brovarone, A.; Tumiati, S.; Piccoli, F.; Ague, J. J.; Connolly, J. A. & Beyssac, O. (2020). Fluid-mediated selective
1012 dissolution of subducting carbonaceous material: Implications for carbon recycling and fluid fluxes at forearc depths.
1013 Chemical Geology, 2020, 549, 119682

1014 Von Raumer, J., Abrecht, J., Bussy, F., Lombardo, B., Menot, R. P., & Schaltegger, U. (1999). The Paleozoic metamorphic
1015 evolution of the Alpine external massifs. Schweizerische Mineralogische und Petrographische Mitteilungen, 79, 5-
1016 22.

Whitney, D.L., Fornash, K.F., Kang, P., Ghent, E.D., Martin, L., Okay, A.I., Vitale Brovarone, A. (2020). Lawsonite composition and zoning as tracers of subduction processes: A global review. Lithos 370–371, 105636. https://doi.org/10.1016/j.lithos.2020.105636

**Fig. 1**

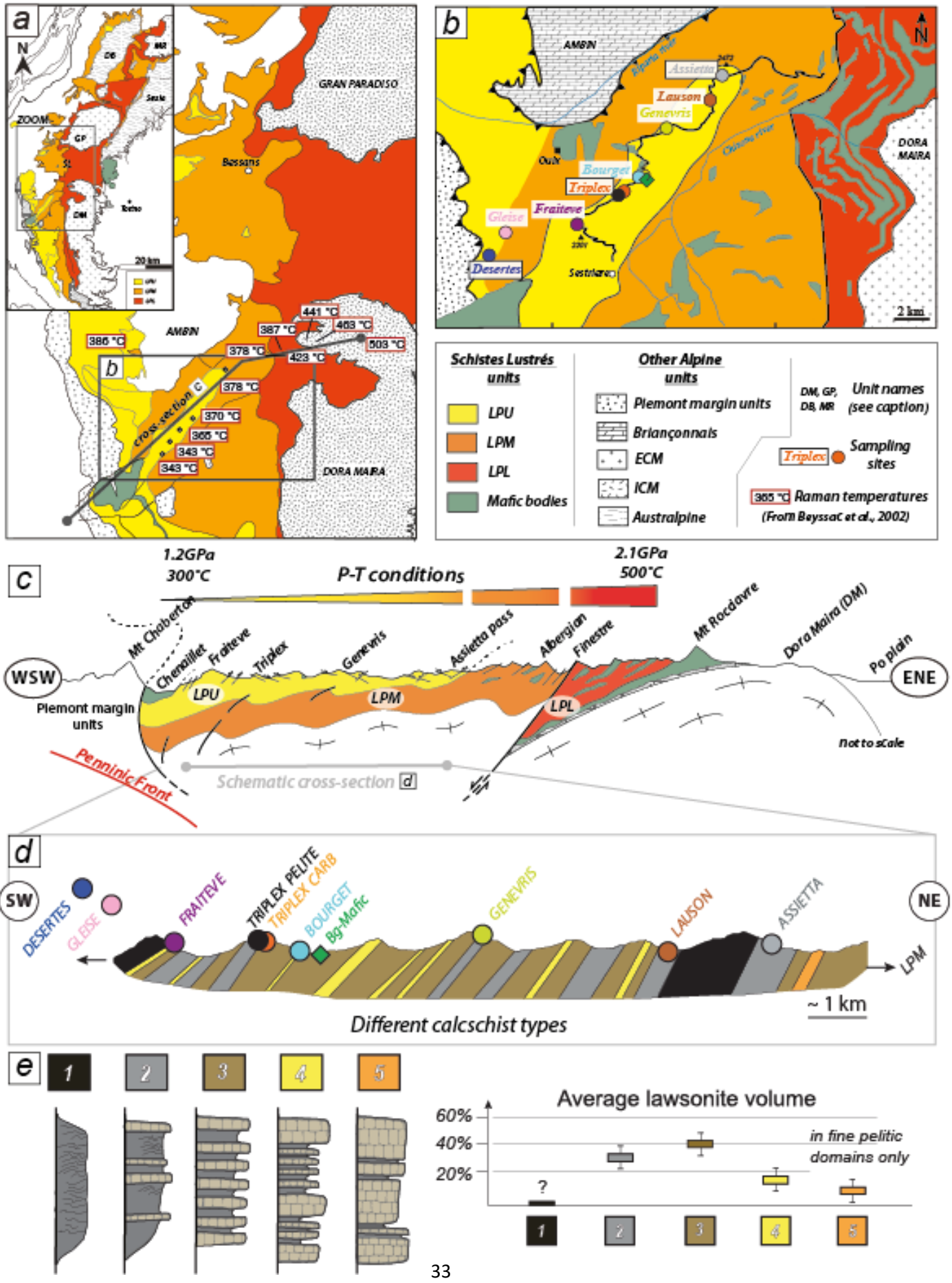
a
N
ZOOM
GP
DB
MR
DM
20 km
GRAN PARADISO
Bassans
AMBIN
DORA MAIRA
441 °C
463 °C
387 °C
386 °C
378 °C
503 °C
423 °C
378 °C
370 °C
365 °C
343 °C
343 °C
cross-section c
b
b
AMBIN
Assietta
Lauson
Genevris
Ouille
Bourget
Triplex
Fraiteve
Gleise
Desertes
Sestriere
DORA MAIRA
2 km
Schistes Lustrés units
LPU
LPM
LPL
Mafic bodies
Other Alpine units
Piemont margin units
Briançonnais
ECM
ICM
Australpine
DM, GP, DB, MR
Unit names (see caption)
Triplex
Sampling sites
365 °C
Raman temperatures
(From Beyssac et al., 2002)
c
1.2GPa
300°C
P-T conditions
2.1GPa
500°C
Mt Chaberton
Chenaillet
Fraiteve
Triplex
Genevris
Assietta pass
Albergian
Finestre
Mt Rocciavre
Dora Maira (DM)
Po plain
WSW
ENE
Piemont margin units
LPU
LPM
LPL
Not to scale
Penninic Front
Schematic cross-section d
d
SW
NE
DESERTES
GLEISE
FRAITEVE
TRIPLEX PELITE
TRIPLEX CARB
BOURGET
Bg-Mafic
GENEVRIS
LAUSON
ASSIETTA
LPM
~ 1 km
Different calcschist types
e
1
2
3
4
5
Average lawsonite volume
60%
40%
20%
in fine pelitic domains only
?
1
2
3
4
5

**Fig. 2**

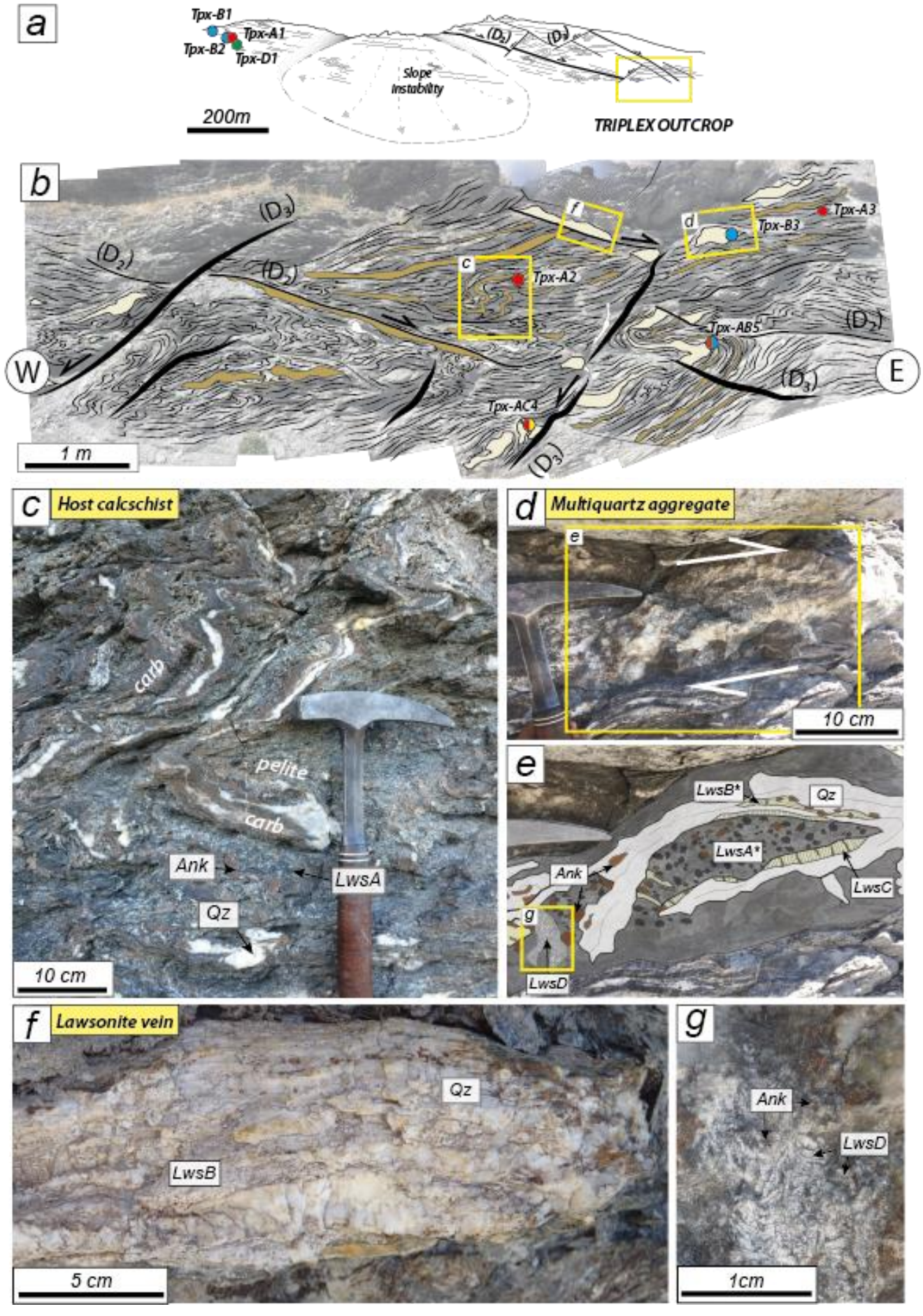
a
Tpx-B1
Tpx-A1
Tpx-B2
Tpx-D1
(D2)
(D3)
Slope instability
200m
TRIPLEX OUTCROP
b
(D3)
(D2)
(D2)
f
d
Tpx-A3
Tpx-B3
c
Tpx-A2
Tpx-AB5
(D2)
W
E
(D3)
Tpx-AC4
(D3)
1 m
c Host calcschist
carb
pelite
carb
Ank
LwsA
Qz
10 cm
d Multiquartz aggregate
e
10 cm
e
LwsB*
Qz
LwsA*
Ank
LwsC
g
LwsD
f Lawsonite vein
Qz
LwsB
5 cm
g
Ank
LwsD
1cm

**Fig. 3**

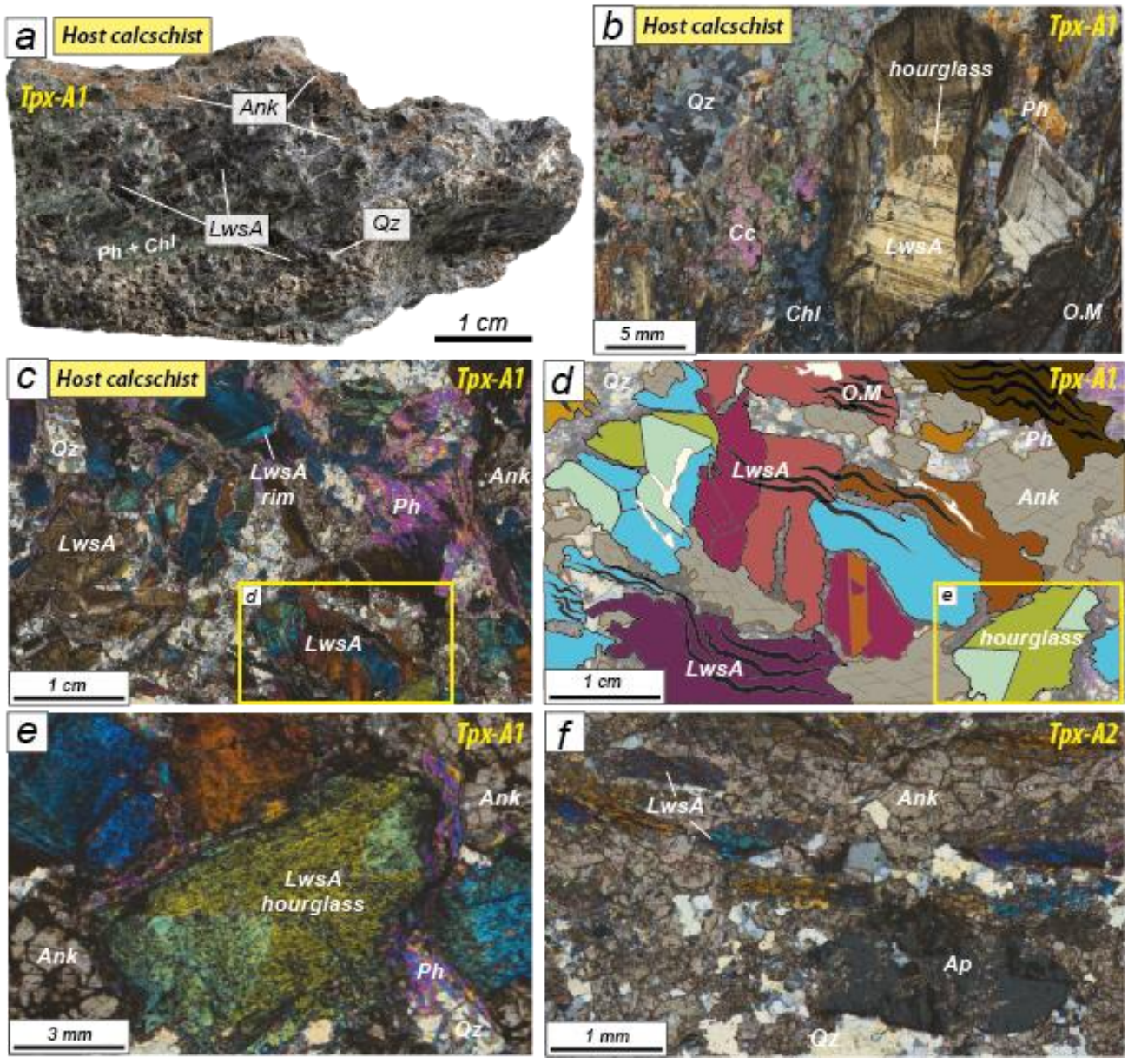
a
Host calcschist
Tpx-A1
Ank
LwsA
Qz
Ph + Chl
1 cm
b
Host calcschist
Tpx-A1
hourglass
Qz
Ph
Cc
LwsA
Chl
O.M
5 mm
c
Host calcschist
Tpx-A1
Qz
LwsA rim
Ank
Ph
LwsA
d
LwsA
1 cm
d
Qz
O.M
Tpx-A1
Ph
LwsA
Ank
e
hourglass
LwsA
1 cm
e
Tpx-A1
Ank
LwsA hourglass
Ank
Ph
Qz
3 mm
f
Tpx-A2
LwsA
Ank
Ap
Qz
1 mm

**Fig. 4**

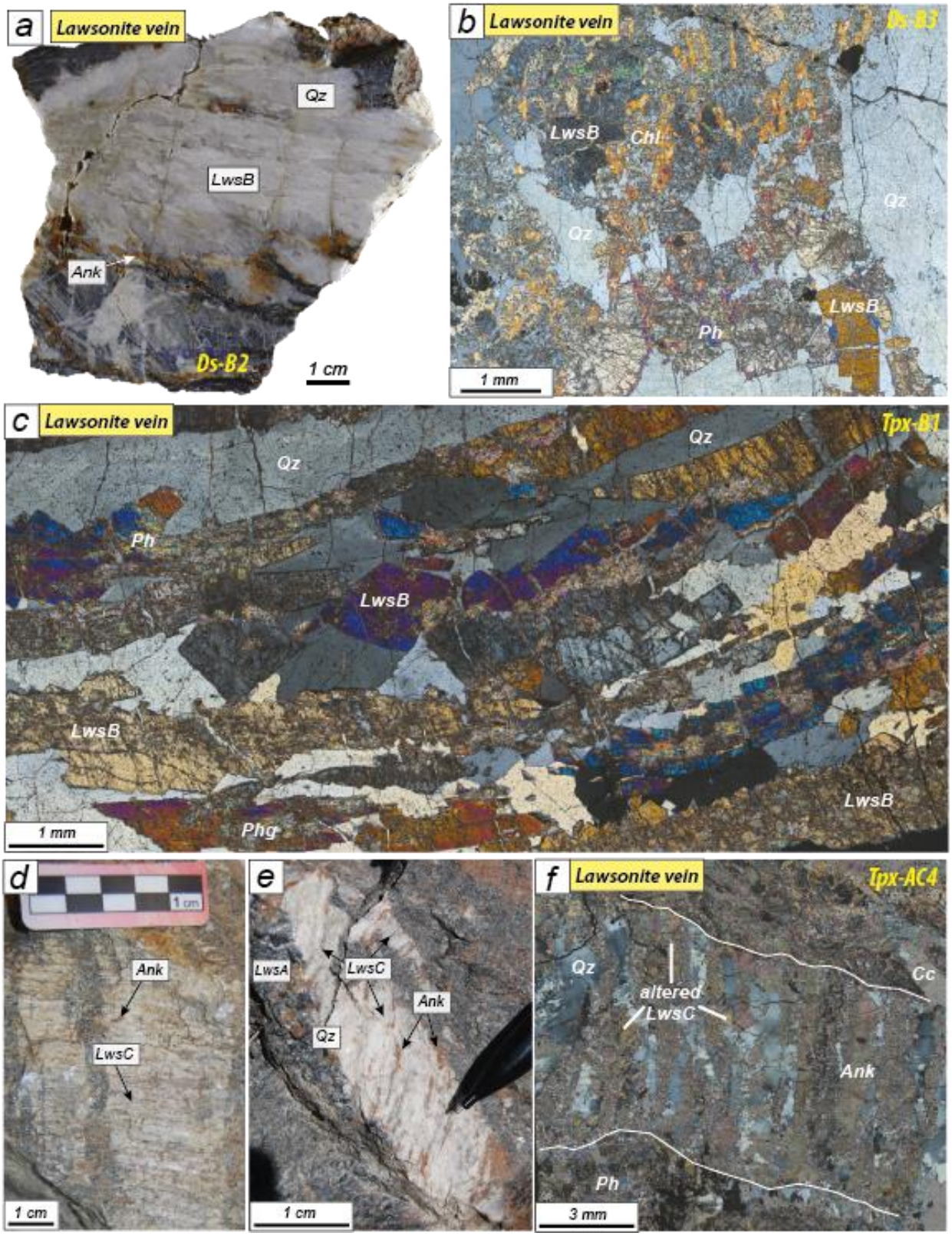
a
Lawsonite vein
Qz
LwsB
Ank
Ds-B2
1 cm
b
Lawsonite vein
Ds-B3
LwsB
Chl
Qz
Qz
Qz
LwsB
Ph
1 mm
c
Lawsonite vein
Tpx-B1
Qz
Qz
Qz
Ph
LwsB
LwsB
LwsB
1 mm
Phg
d
Ank
LwsC
1 cm
e
LwsA
LwsC
Ank
Qz
1 cm
f
Lawsonite vein
Tpx-AC4
Qz
Cc
altered
LwsC
Ank
Ph
3 mm

**Fig. 5**

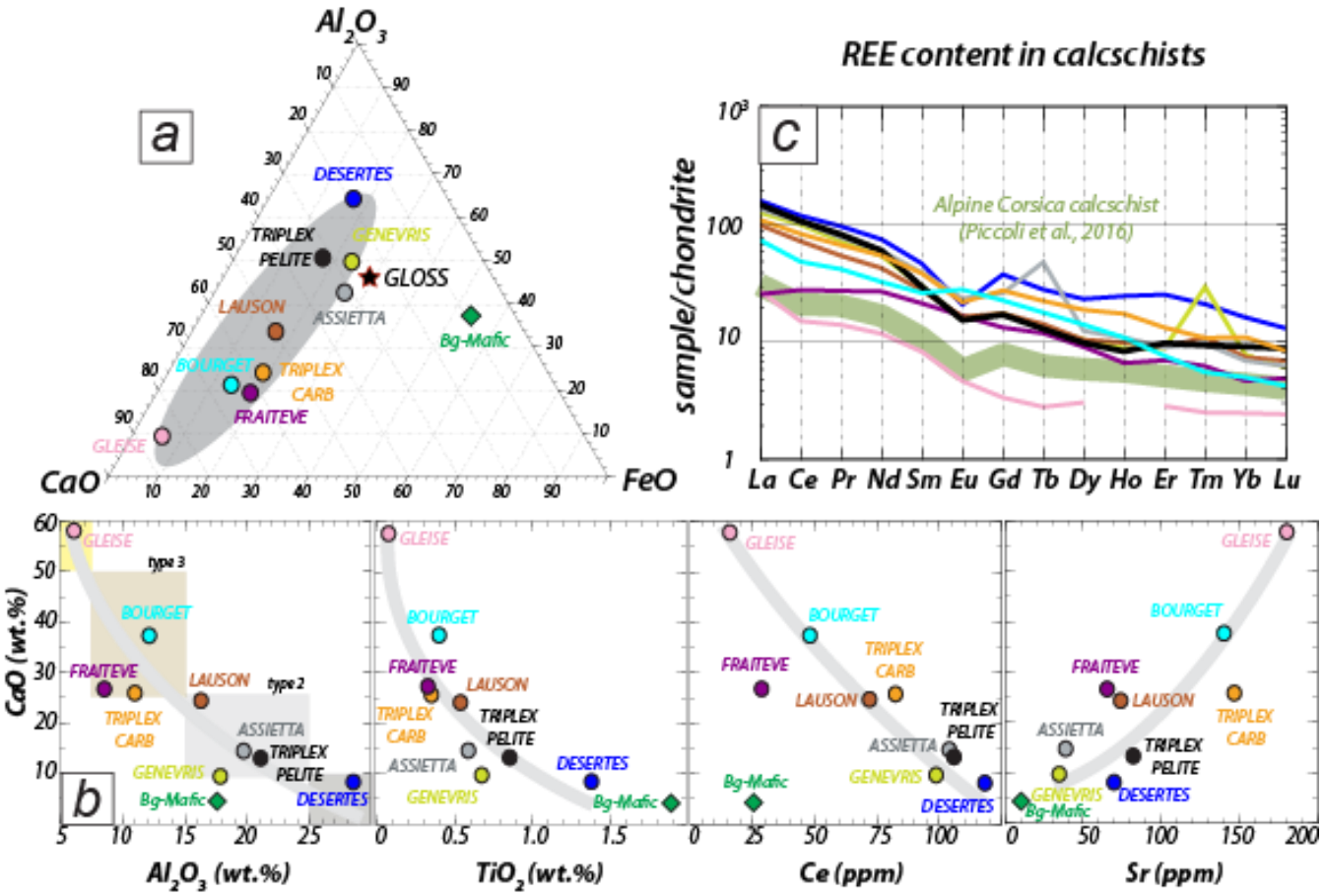
a
$Al_2O_3$
CaO
FeO
DESERTES
TRIPLEX PELITE
GENEVRIS
GLOSS
LAUSON
ASSIETTA
Bg-Mafic
BOURGET
TRIPLEX CARB
FRAITEVE
GLEISE
c
REE content in calcschists
sample/chondrite
Alpine Corsica calcschist
(Piccoli et al., 2016)
La Ce Pr Nd Sm Eu Gd Tb Dy Ho Er Tm Yb Lu
b
CaO (wt.%)
type 3
type 2
$Al_2O_3$ (wt.%)
$TiO_2$(wt.%)
Ce (ppm)
Sr (ppm)

**Fig. 6**

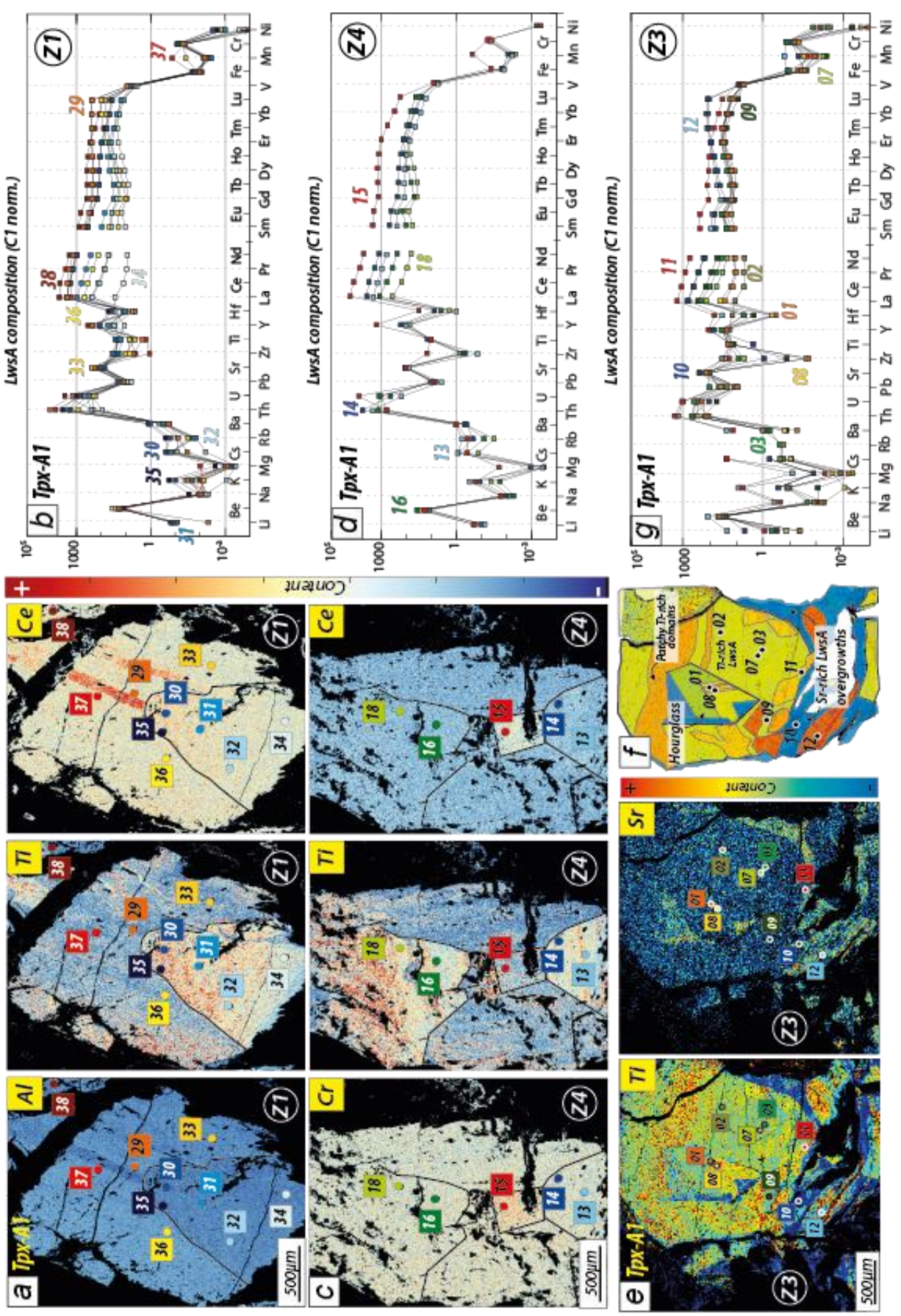
a Tpx-A1
Al
Ti
Ce
Cr
Sr
b Tpx-A1
d Tpx-A1
g Tpx-A1
e Tpx-A1
f
LwsA composition (C1 norm.)
Z1
Z3
Z4
Content
Hourglass
Patchy Th-rich domains
Th-rich LwsA
Sr-rich LwsA overgrowths
500µm

**Fig. 7**

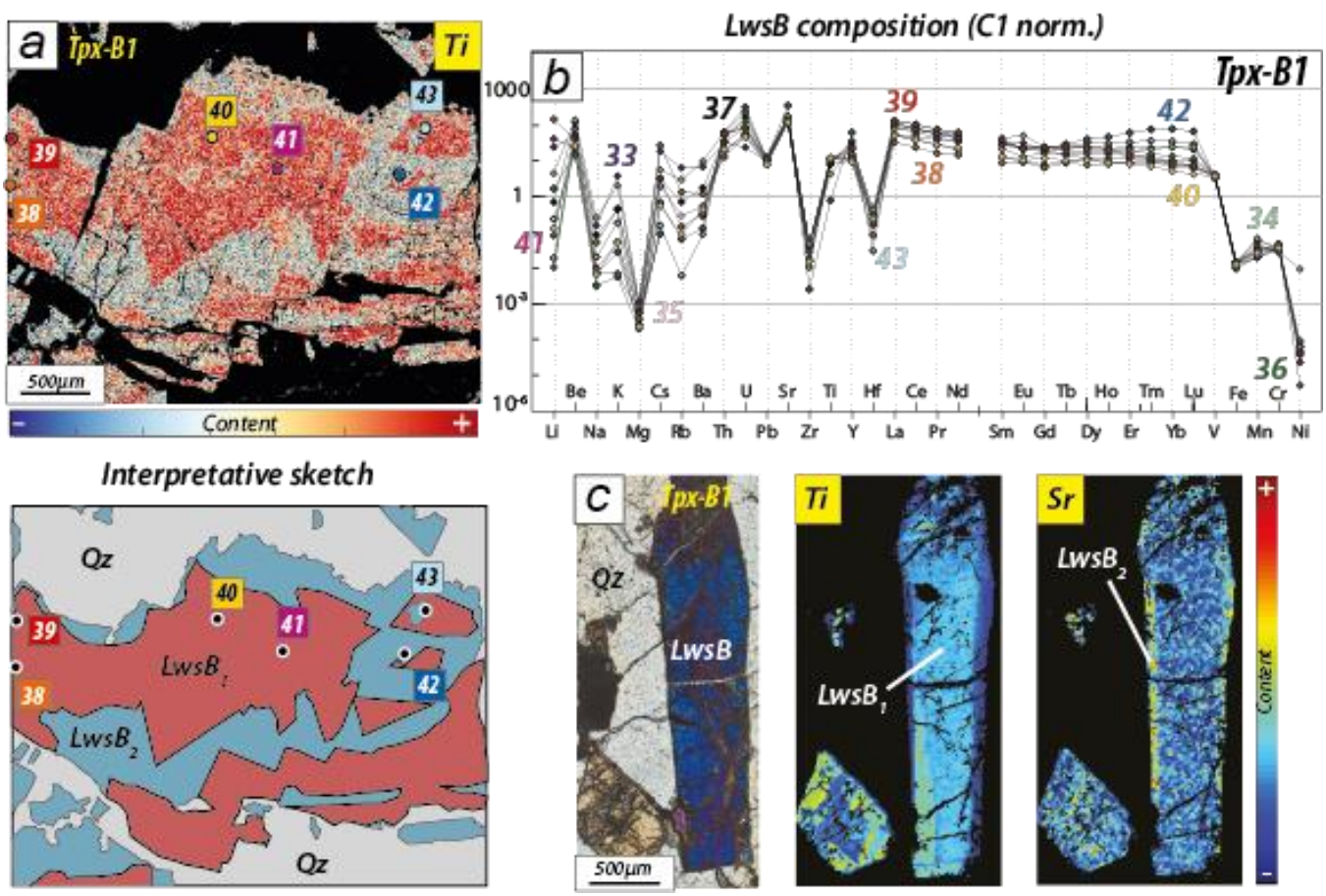
a
Tpx-B1
Ti
40
41
43
39
38
42
500µm
Content
LwsB composition (C1 norm.)
b
Tpx-B1
1000
1
10⁻³
10⁻⁶
37
39
33
38
42
40
41
43
34
35
36
Be K Cs Ba U Sr Tl Hf Ce Nd Eu Tb Ho Tm Lu Fe Cr
Li Na Mg Rb Th Pb Zr Y La Pr Sm Gd Dy Er Yb V Mn Ni
Interpretative sketch
Qz
40
43
39
41
LwsB1
38
42
LwsB2
Qz
C
Tpx-B1
Qz
LwsB
500µm
Ti
LwsB1
Sr
LwsB2
Content

**Fig. 8**

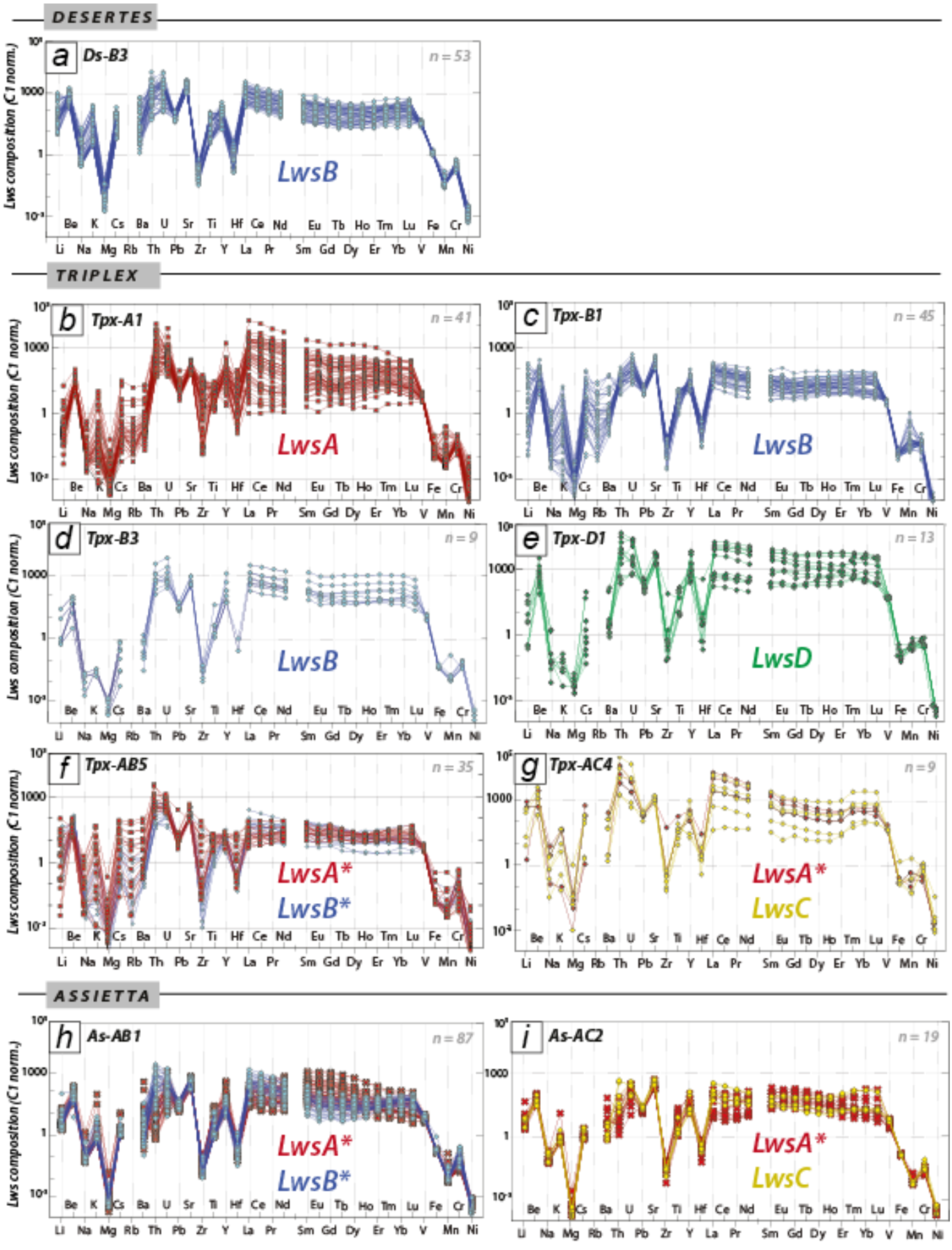
DESERTES
a Ds-B3
n = 53
LwsB
TRIPLEX
b Tpx-A1
n = 41
LwsA
c Tpx-B1
n = 45
LwsB
d Tpx-B3
n = 9
LwsB
e Tpx-D1
n = 13
LwsD
f Tpx-AB5
n = 35
LwsA*
LwsB*
g Tpx-AC4
n = 9
LwsA*
LwsC
ASSIETTA
h As-AB1
n = 87
LwsA*
LwsB*
i As-AC2
n = 19
LwsA*
LwsC
Lws composition (C1 norm.)
Be K Cs Ba U Sr Ti Hf Ce Nd Eu Tb Ho Tm Lu Fe Cr
Li Na Mg Rb Th Pb Zr Y La Pr Sm Gd Dy Er Yb V Mn Ni

**Fig. 9**

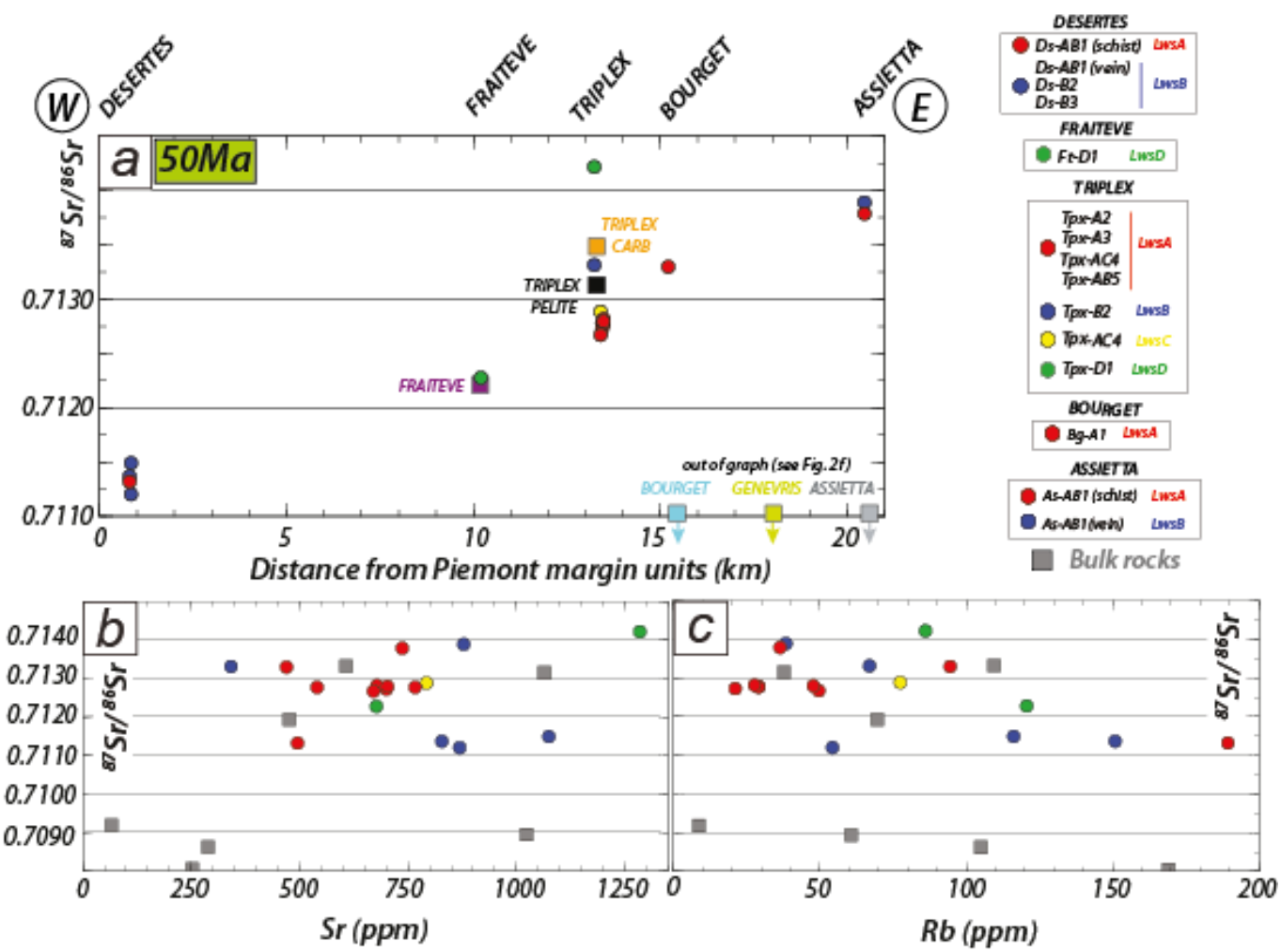
W
DESERTES
FRAITEVE
TRIPLEX
BOURGET
ASSIETTA
E
a
50Ma
87Sr/86Sr
0.7130
0.7120
0.7110
TRIPLEX
CARB
TRIPLEX
PELITE
FRAITEVE
out of graph (see Fig. 2f)
BOURGET
GENEVRIS
ASSIETTA
0
5
10
15
20
Distance from Piemont margin units (km)
DESERTES
Ds-AB1 (schist)
LwsA
Ds-AB1 (vein)
Ds-B2
Ds-B3
LwsB
FRAITEVE
Ft-D1
LwsD
TRIPLEX
Tpx-A2
Tpx-A3
Tpx-AC4
Tpx-AB5
LwsA
Tpx-B2
LwsB
Tpx-AC4
LwsC
Tpx-D1
LwsD
BOURGET
Bg-A1
LwsA
ASSIETTA
As-AB1 (schist)
LwsA
As-AB1 (vein)
LwsB
Bulk rocks
b
0.7140
0.7130
0.7120
0.7110
0.7100
0.7090
87Sr/86Sr
0
250
500
750
1000
1250
Sr (ppm)
c
87Sr/86Sr
0
50
100
150
200
Rb (ppm)

**Fig. 10**

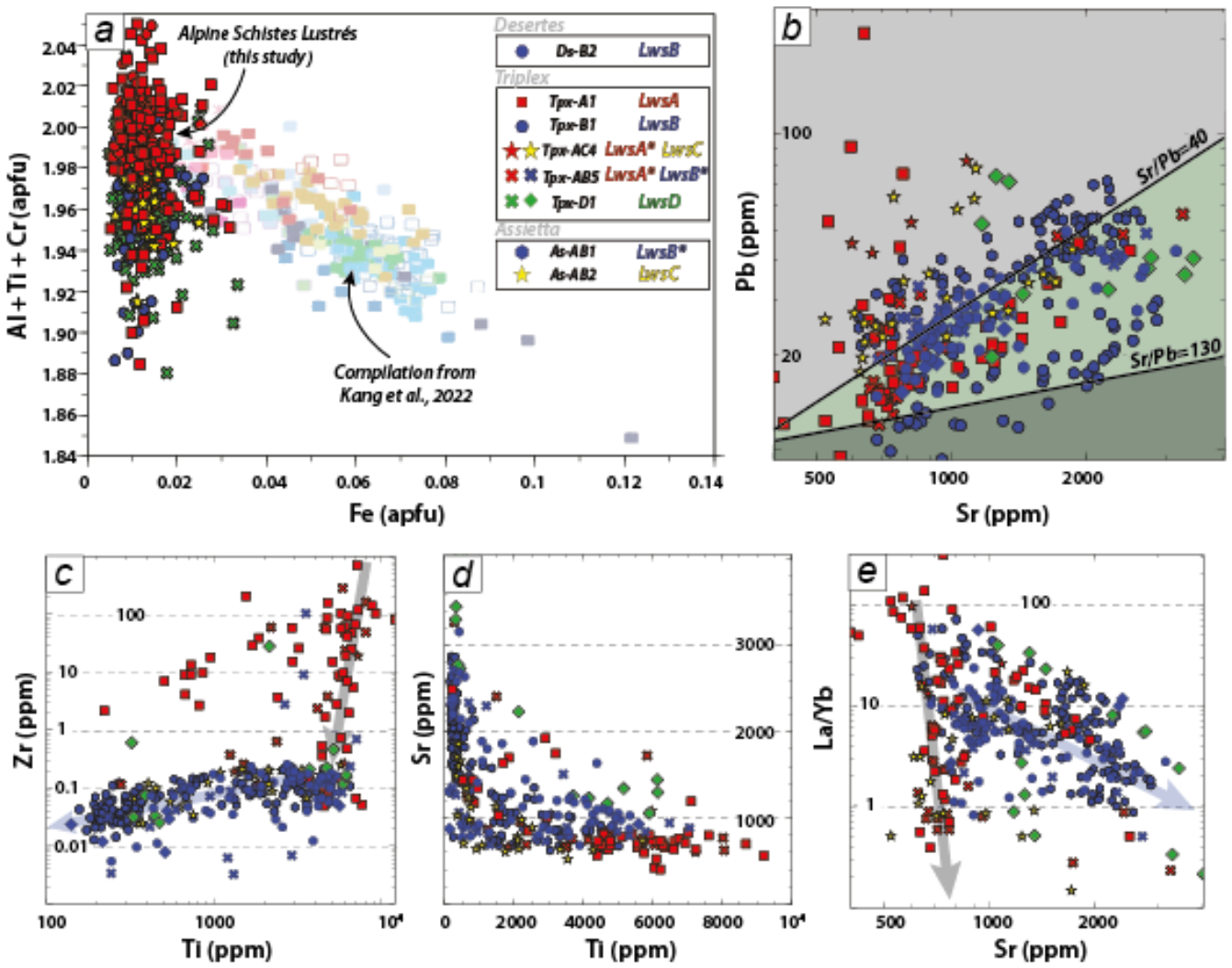
a
Alpine Schistes Lustrés (this study)
Compilation from Kang et al., 2022
Desertes
Ds-B2 LwsB
Triplex
Tpx-A1 LwsA
Tpx-B1 LwsB
Tpx-AC4 LwsA* LwsC
Tpx-AB5 LwsA* LwsB*
Tpx-D1 LwsD
Assietta
As-AB1 LwsB*
As-AB2 LwsC
Al+Ti+Cr (apfu)
Fe (apfu)
b
Pb (ppm)
Sr (ppm)
Sr/Pb=40
Sr/Pb=130
c
Zr (ppm)
Ti (ppm)
d
Sr (ppm)
Ti (ppm)
e
La/Yb
Sr (ppm)

**Fig. 11**

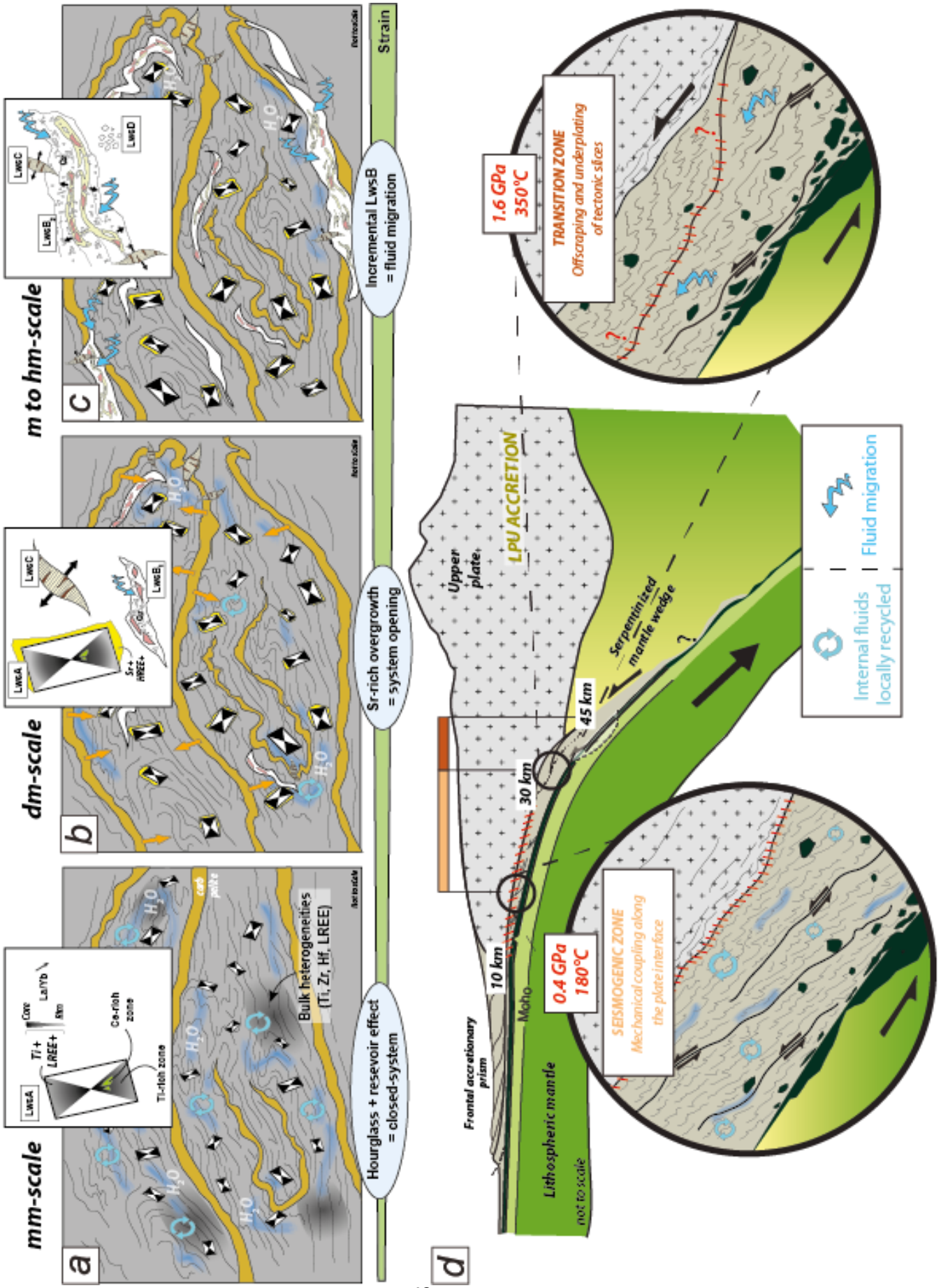
mm-scale
dm-scale
m to hm-scale
a
b
c
d
LwsA
LwsB1
LwsC
LwsD
Ti+ LREE+
Core
Rim
Ce-rich zone
Ti-rich zone
Bulk heterogeneities (Ti, Zr, Hf, LREE)
Sr+ HREE+
Gt
Hourglass + resevoir effect = closed-system
Sr-rich overgrowth = system opening
Incremental LwsB = fluid migration
Strain
1.6 GPa 350°C
TRANSITION ZONE
Offscraping and underplating of tectonic slices
0.4 GPa 180°C
SEISMOGENIC ZONE
Mechanical coupling along the plate interface
Upper plate
LPU ACCRETION
Serpentinized mantle wedge
45 km
30 km
10 km
Moho
Frontal accretionary prism
Lithospheric mantle
not to scale
Internal fluids locally recycled
Fluid migration

# Figures captions

## Fig1. Geological settings

**(a)** Simplified geological map of the Western Alps modified after Herviou et al. (2022). GP: Gran Paradiso; DB: Dent Blanche; MR: Monte Rosa; DM: Dora Maira. SL units are in yellow for upper units (LPU), orange for middle units (LPM) and red for lower units (LPL). Raman spectra on carbonaceous material temperatures of Beyssac et al. (2002) are reported. **(b)** Close-up of simplified geological map of the zone of interest. Mafic bodies are shown in green. Bulk rock samples collected along the Strada dell'Assietta transect are shown as colored circles and diamonds. **(c)** WSW-ENE simplified cross section of the SL illustrating the geometry and distribution of the stacked units of the SL. Peak pressure-temperature conditions from west to east are reported according to Agard et al. (2001). **(d)** Simplified cross-section of the transect between Fraiteve and the Assietta pass (see Fig. 1). The color code (schematized in (e)) indicates the rock type, from 1 (pelite) to 5 (carbonate with very few pelite layers). Samples are located and labeled along the transect (colored circles). **(e)** Average volumetric content of lawsonite (regardless of lawsonite type) for each lithology.

## Fig2. Several types of lawsonite observed at Triplex

**(a)** Schematized Triplex outcrop where main deformation structures (D2, D3) are highlighted. Samples Tpx-A1, Tpx-B1, Tpx-B2 and Tpx-D1 are located with colored dots. **(b)** Triplex outcrop photograph overlaid by a sketch of the structural framework with locations of samples Tpx-A2, Tpx-A3, Tpx-B3, Tpx-AC4 and Tpx-AB5. Carbonate horizons are in light brown and lawsonite-bearing veins in white. Yellow rectangles locate following subfigures. **(c)** Field photograph of intensely folded metasediments composed of centimeter-scale alternations of pelite-rich and carbonate-rich domains (carb). LwsA black prisms are abundant in pelite-rich layers and associated with ankerite (Ank). Quartz (Qz) and thin calcite veins are numerous. **(d)** Centimeter-scale multiquartz aggregate in which all lawsonite types are observed, schematically interpreted in **(e).** In these aggregates, clasts of pelitic schists are often embedded in LwsB bearing veins ductilely deformed. **(f)** Isolated quartz-rich LwsB vein in the SL metasediments. **(g)** LwsD in the host calcschist, next to LwsB-bearing veins.

## Fig3. Mineralogy of LwsA-bearing host calcschists

**(a)** Hand specimen of a LwsA-bearing calcschist (Tpx-A1) with LwsA as black prisms, associated with ankerite and quartz. Note retrograde chlorite (Chl) and phengite (Ph replacing lawsonite. **(b), (c)** Photographs of the associated thin section (Tpx-A1) underlining the high abundance of LwsA in the calcschist. Lawsonite crystal cores contain abundant organic matter (OM) inclusions. **(d)** Interpretative sketch of the area in yellow rectangle in (c) highlighting hourglass zonations commonly observed in

LwsA. **(e)** Close-up view of a hourglass-zoned LwsA associated with quartz and ankerite and partly retrogressed in phengite. **(f)** LwsA located in the carbonate horizon of sample Tpx-A2 where ankerite is predominant and where apatite crystals have been observed, a rare accessory mineral.

## Fig4. Mineralogy of LwsB and LwsC-bearing veins

**(a)** Hand specimen of a LwsB-bearing vein (Ds-B2). LwsB cream-colored crystals is associated with quartz and grows as fibers elongated parallel to the vein selvages. **(b)**, **(c)** Photographs of Qz and LwsB-bearing vein thin sections (Tpx-B3, Tpx-B1, cross-polarized). These lawsonite crystals never contain OM inclusions but are often retrogressed into Ph + Chl mixture. **(d)**, **(e)** LwsC vein in the calcschists, with ankerite and quartz. **(f)** Photograph of the sample Tpx-AC4 thin section centered on a LwsC-bearing vein. LwsC are often pseudomorphed into a mixture of phengite, chlorite and calcite, complicating geochemical analysis.

## Fig5. Representative geology and whole rock geochemistry

**(a)** $Al_2O_3$, FeO, CaO relative weight fractions in bulk rock samples. Average pelite composition is represented in gray and the GLOSS composition is shown for reference. **(b)** Major and trace element contents for bulk rocks. From left to right: $Al_2O_3$ (wt. %), $TiO_2$ (wt. %), Ce (ppm) and Sr (ppm) contents against the CaO (wt. %) content, the latter reflecting carbonate proportion. **(c)** REE concentrations of the calcschists, normalized to chondritic values from McDonough and Sun (1995). Alpine Corsican calcschists from Piccoli et al. (2016) are reported for comparison.

## Fig6. Incremental growth recorded in host calcschist (Tpx-A1)

**(a)** Al, Ti and Ce chemical maps (SEM) of a LwsA crystal from Tpx-A1 (map C1). These maps highlight hourglass zoning. **(b)** Spider diagram showing element contents normalized to C1 chondrite, for ablation spots 29 to 38 located on maps from Fig. 7a. **(c)** Cr, Ti and Ce chemical maps (SEM) of a LwsA crystal from Tpx-A1 (map C4). Hourglass zoning is best seen on the Ti map. **(d)** Spider diagrams showing element contents normalized to C1 chondrite, for ablation spots 13 to 18 located on maps from Fig. 7c. **(e)** Ti and Sr chemical maps (EPMA) of a LwsA crystal from Tpx-A1 (map C3). These maps highlight a complex history of incremental growth interpreted in sketch **(f).** The crystal core shows hourglass zoning entrapped in a Ti-rich domain presenting a patchy distribution overgrown by a Sr-rich, Ti-depleted rim. **(g)** Spider diagram showing element contents normalized to C1 chondrite (ablation spots 01 to 12 located in Fig.7e).

## Fig7. Incremental growth recorded in quartz-rich LwsB-bearing vein (Tpx-B1)

**(a)** Ti chemical map (SEM) of a LwsB crystal from Tpx-B1 (map C3). This map highlights angular Ti-rich domains in LwsB cores, rimmed by Ti-poor lawsonite, interpreted as incremental growth during the vein formation. Below**:** interpretative sketch of LwsB incremental growth in the quartz-rich vein. $LwsB_1$ cores are Ti-enriched whereas $LwsB_2$ rims are Ti depleted. **(b)** Spider diagram with element contents normalized to C1 chondrite (ablation spots 38 to 43 located in Fig.8a). **(c)** Optical microscopy, Ti and Sr chemical maps (SEM) of a LwsB crystal from Tpx-B1.

## Fig8. Trace element patterns of lawsonite

Spider diagrams of 35 elements analyzed by laser-ablation ICP-MS in the lawsonite types encountered in the field. All 311 spectra are normalized to C1 chondrite from McDonough and Sun (1995) and are presented by sampling sites and lawsonite types to ease reading. The color code refers to the lawsonite type even when encountered in the same sample (in multiquartz aggregates: Fig. 10f-i).

## Fig9. Strontium isotopic signal of lawsonites

**(a)** $^{87}Sr/^{86}Sr$ ratios in lawsonite separates, plotted against the sample distance to the Piemont margin units westward. Sampling locations are reported in Fig. 1b. The different types of lawsonite are highlighted by specific colors (LwsA: red, LwsB: dark blue; LwsC: yellow; LwsD: green). TIMS $^{87}Sr/^{86}Sr$ data have been corrected considering an age of crystallization of 50 Ma for lawsonite. Estimated errors are smaller than point size. All the data and corrections are available in Table 8. **(b, c)** $^{87}Sr/^{86}Sr$ ratios plotted against Sr **(b)** and Rb **(c)** concentrations (ICP-MS).

## Fig10. Geochemical correlations

**(a)** Al + Ti + Cr content (a.p.f.u.) in function of the Fe (a.p.f.u.) content of the Alpine Schistes Lustrés lawsonites compared to the compilation of worldwide lawsonites collected in different geodynamical contexts after Kang et al. (2022). The samples are detailed in the legend and color-coded to identify the different lawsonite types. **(b)** Sr content (in ppm) plotted against Pb content (in ppm). The three highlighted domains (gray, light and dark green) are plotted according to Whitney et al. (2020) where these Pb/Sr ratios have been inferred to discriminate sedimentary lawsonite from mafic rocks lawsonite. **(c)** Ti content (in ppm) plotted against Zr content (in ppm). **(d)** Ti content (in ppm) plotted against Sr content (in ppm). **(e)** La/Yb ratio plotted against Sr content (in ppm). **(f)** Yb content (in ppm) plotted against Sr content (in ppm).

## Fig11. Scenario of fluid circulation and element mobility length-scale

**(a)** Early crystallization of LwsA in the pelitic schists results from restricted, mm-scale element migration through locally released fluid. LwsA zoning patterns reveal out-of-equilibrium growth processes occurring at low temperature (i.e., sluggish diffusivity) in a rather closed system: hourglass zoning, growth zoning (i.e., reservoir effect) and interface-coupled dissolution-precipitation processes (i.e., patchy zoning) affecting poorly mobile elements (Ti, LREE, Cr). **(b)** Along burial, increasing temperature, deformation and fluid release contribute to progressively increase the scale of fluid-rock interactions. Sr-rich LwsA overgrowths and local homogeneity of Sr isotopic ratios suggest that fluid homogenization between pelitic and carbonate-rich layers remained restricted to the dm-scale. LwsC tension gashes were likely fed by local element transfer. **(c)** Close to peak burial conditions, the transiently connected vein network allowed fluid homogenization at the m- to hm-scale (sub-unit scale). Incremental growth of LwsB veins with Sr-rich rims records the progressive increase of element mobility length-scale. LwsB incremental veins and multiquartz aggregates acted as drains for fluids. However, the lack of homogeneity of Sr isotopic signature suggests that the SL unit remained a closed-system and did not record massive infiltration of external fluids. **(d)** Integration of this petrological scenario at subduction-zone scale. The P-T conditions correspond to the LwsA massive formation (around 0.4 GPa, 180°C; Lefeuvre et al., 2020). At this stage, fluids are locally produced through metamorphic dehydration reactions and are internally recycled forming large amounts of lawsonite. Incremental formation of lawsonite veins induces progressive opening of the system, mass transfer likely reaching the hm-scale. Reaching peak burial (1.6 GPa, 350°C; Agard et al., 2001), the SL units were scrapped off and progressively stacked to the upper plate allowing their later exhumation. This implies a shift in the mechanical behavior of the sedimentary pile.

# Table captions

**(tables and supplementary materials are available contacting the corresponding author)**

### Table 1. Sample characterization

Samples investigated here, sorted by locations (Desertes, Fraiteve, Bourget, Triplex, Assietta). Lawsonite types are provided, together with the mineralogy, performed analyses and GPS coordinates. LwsA* and LwsB* relate to multiquartz aggregates. Mineral proportions are given with a qualitative scale ('-': not seen; '+': rarely seen; '++': present in the entire thin section in proportions < 50 %; '+++': ubiquitous).

**Table 2. Bulk rock geochemistry (ICP-OES and ICP-MS)**

Bulk rock analyses. Major elements are expressed in weight %, trace elements in ppm. Bulk rocks are calcschists, except for sample Bg-Mafic which is a pillow breccia embedded in the Bourget calcschists.

**Table 3. Major elements of LwsA from microprobe analysis**

Weight percentages of investigated oxides for each analysis made on LwsA crystals. $TiO_2$, SrO and $Cr_2O_3$ are given with a greater precision because of special analytical conditions for these elements (see methods). B.d.l.: below detection limits. The formula units are calculated on 8 oxygen atoms.

**Table 4. Major elements of LwsB from microprobe analysis**

Weight percentages of investigated oxides for each analysis made on LwsB crystals. $TiO_2$, SrO and $Cr_2O_3$ are given with a greater precision because of special analytical conditions for these elements (see methods). B.d.l.: below detection limits. The formula units are calculated on 8 oxygen atoms.

**Table 5. Major elements of LwsC from microprobe analysis**

Weight percentages of investigated oxides for each analysis made on LwsC crystals. $TiO_2$, SrO and $Cr_2O_3$ are given with a greater precision because of special analytical conditions for these elements (see methods). B.d.l.: below detection limits. The formula units are calculated on 8 oxygen atoms.

**Table 6. Major elements of LwsD from microprobe analysis**

Weight percentages of investigated oxides for each analysis made on LwsD crystals. $TiO_2$, SrO and $Cr_2O_3$ are given with a greater precision because of special analytical conditions for these elements (see methods). B.d.l.: below detection limits. The formula units are calculated on 8 oxygen atoms.

**Table 7. Lawsonite geochemistry (LA-ICP-MS/MS)**

Trace element concentrations (in ppm) of different types of lawsonite obtained by laser ablation ICP-MS/MS.

**Table 8. Strontium isotopic ratios (TIMS)**

Strontium isotopic ratios of bulk rocks and lawsonite separates. The Rb and Sr concentrations (in ppm) and $^{87}Rb/^{86}Sr$ ratios measured with ICP-MS/MS have been added to the dataset. The $^{87}Sr/^{86}Sr$ have been corrected assuming three different crystallization ages for the lawsonite: 40 Ma, 50 Ma and 60 Ma.

# Supplementary material captions

## Sup. Mat. 1. Mineralogy of LwsA* and LwsB*-bearing samples in multiquartz aggregates

**(a**) Multiquartz aggregate observed in the Triplex area with coalescent LwsB-bearing veins. Fragments of the host calcschists are included in the veins, as schematized on **(b)**. **(c)** Hand specimen of a multiquartz aggregate (Tpx-AC4) where schistose clasts containing LwsA* are embedded in a LwsB*-bearing quartz-rich vein. LwsB* crystals are sometimes associated with ankerite where located next to the pelitic fragments. **(d)** LwsB* crystals thin section illustrating elongation of lawsonite fibers (polarized light). In this sample (Assietta, As-AB1), LwsB* crystals are essentially associated with quartz and retrogressed to phengite and chlorite. **(e)** Photograph of the Tpx-AC4 centered on a calcschist clast where LwsA* are ubiquitous, presenting the same microstructures as LwsA: association with ankerite and quartz, inclusions of OM in the cores and OM-free rims. (f) Field photograph of a multiquartz aggregate presenting LwsA* in a host rock fragment and a LwsC-bearing vein. **(g)** Close-up view of the sharp interface between LwsA* bearing clasts and the LwsC bearing vein (As-AC2). LwsC crystals grow perpendicularly to the vein selvages (polarized light).

## Sup. Mat. 2. Lawsonite separation protocol

Schematized protocol followed in this study to isolate lawsonite crystals from the bulk rocks. Each step is specified from crushing to the hand picking. SEM imaging was used to ensure purity after heavy liquids and Frantz magnetic separation.

## Sup. Mat. 3. Univalent contamination of lawsonite by white micas

Mica contamination evidenced by positive correlations between K (ppm) and several other elements (Na, Ba, Rb, Li and Cs). Symbols code for lawsonite types.

## Sup. Mat. 4. Distribution of trace elements in multiquartz aggregates (LwsA* & LwsB*)

**(a)** Ti chemical map (EPMA) of a LwsB* crystal from Tpx-AB5 (zone C1, see location on the thick section in Sup.Mat. 4). Ti-rich cores rimmed by Ti-poor borders suggest incremental growth during vein formation. Spots show locations of the laser ablation analyses (Fig.9b). **(b)** Spider diagram of C1 chondrite-normalized element contents for spots 29 to 35 (localized in (a). **(c)** Ti, Cr and Ce chemical maps (EPMA) of a LwsA* crystal from Tpx-AB5 (zone C3, see location on the thick section in Sup.Mat. 4). **(d)** Plane polarized photography of LwsA* highlighting OM-enriched core surrounded by a clear outer rim. **(e)** Spider diagram of C1 chondrite-normalized element contents for spots 02 to 09 localized in (c) and (d). **(f)** Optical microscopy, Ti and Sr maps (SEM) centered on a LwsC-bearing vein and the

LwsA*-bearing clast. Note that the OM and the Ti are restricted to the LwsA* crystal, illustrating hourglass zonation.

## Sup. Mat. 5. Strontium isotopic "errorchron"

$^{87}Sr/^{86}Sr$ versus $^{87}Rb/^{86}Sr$ for both bulk rocks and lawsonite separates collected at Triplex. The respective errors are reported on the graphic.